CHARACTERIZING THE OPTICAL PERFORMANCE OF A SPACED-BASED STELLAR OCCULTATION SYSTEM USING APERTURE FORMATION DESIGN

A Thesis

by

KRISTIN DANETTE NICHOLS

Submitted to the Office of Graduate and Professional Studies of
Texas A&M University
in partial fulfillment of the requirements for the degree of

MASTER OF SCIENCE

Chair of Committee,	David C. Hyland
Committee Members,	Srivanis Vadali
	Casey Papovich
Head of Department,	Rodney D. Bowersox

August 2015

Major Subject: Aerospace Engineering

ABSTRACT

Stellar occultation is a widely-used method to characterize space-faring objects such as near Earth asteroids, moons and minor planets that pass in front of distant stars. However, the conventional method is limited in that it assumes the occulting object is large enough, or close enough, to cast a sharp shadow. For instance, smaller asteroids that are still large enough to cause severe damage to the Earth upon impact create shadow patterns that are heavily diffracted, making identification and characterization of them difficult.

This thesis develops results supporting novel space-based stellar occultation systems which use shadow diffraction principles to resolve silhouettes of smaller near-Earth asteroids. A formation of light-gathering telescopes is positioned at a halo orbit about the Sun-Earth L_2 libration point. The apertures are positioned in various configurations to better characterize system requirements. The dynamics and control of three candidate geometries are evaluated using the circular restricted three-body problem. Both Proportional Derivative and Linear Quadratic Regulator controls are implemented to maintain the formation geometry with negligible error and very low control forces. Additional parameters such as the size of the array, number of apertures, and overall formation geometry, are discussed to find relationships relating these parameters to the system's optical performance. The most efficient formations are examined and compared, as well as the worst configurations to place performance limits on each geometry.

Three array geometries were analyzed–a linear string of pearls, a circular array, and a Y-shaped array. Overall, the circular array centered at the reference halo orbit shows superior performance because of its insensitivity to the occulting shadow's velocity vector. However, the Y-shaped array is shown to be a viable compromise between the string of pearls and circular arrays by minimizing the number of required apertures while still enabling multiple directions of shadow motion. This work furthers the development of system requirements pertaining to data coverage and aperture positioning for novel space-based stellar occultation systems.

ACKNOWLEDGMENTS

I sincerely thank Dr. David Hyland for his guidance, encouragement, and support while working on my master's degree. It has been an honor and pleasure to work with him, and his brilliance in combining the fields of engineering and science continues to compel me. I would also like to thank my committee members, Dr. Srivanis Vidali and Dr. Casey Papovich, for their time and advice over the last several years. Much of my core classes in graduate school, such as optimal control theory and celestial mechanics, have been taught by Dr. Vadali. He is the type of professor who asks an incredible amount of work from you, but in doing so pushes you beyond what you think possible. Dr. Papovich has been a role model of mine since I studied astronomy with him as an undergraduate. I rediscovered my love of the cosmos in his class and decided to pursue an honors undergraduate research thesis focusing on stability of exoplanetary systems under his guidance. He continues to serve as my mentor and friend.

I'd also like to acknowledge the help of several graduate students, namely Russell Trahan, Amber Wilds, Bharat Mahajan, Chris Spreen, and Allen Ream, who have all aided me greatly in my time in graduate school. I would also like to thank my parents for their encouragement to pursue my education in these many years of college. Their support has been invaluable in the pursuit of my dreams.

TABLE OF CONTENTS

Page

ABSTRACT ii

ACKNOWLEDGMENTS iv

TABLE OF CONTENTS v

LIST OF FIGURES vii

LIST OF TABLES x

NOMENCLATURE xi

1. INTRODUCTION 1
    - 1.1 Background 1
    - 1.2 Objectives and Organization of the Study 3

2. OCCULTATION IMAGING METHOD 5
    - 2.1 Method of Resolving Asteroid Silhouettes 9
        - 2.1.1 Data Collection 10
        - 2.1.2 Phase Retrieval Algorithm 12
        - 2.1.3 Asteroid Characterization 13
    - 2.2 Data Coverage and Aperture Positioning 14

Page
3. THREE-BODY PROBLEM DYNAMICS 22
  3.1 Circular Restricted Three-Body Problem 23
  3.2 Non-dimensional Coordinates and Characteristic Values 24
  3.3 Equations of Motion 26
  3.4 Pseudo-Potential and Jacobi's Constant 28
  3.5 Libration Points 29
  3.6 Stability Analysis 32
  3.7 Periodic Orbits 34

4. CONTROL METHODS 41
  4.1 Control Problem Formulation 41
  4.2 Proportional Derivative Control 42
  4.3 Linear Quadratic Regulator 44
  4.4 Control Implementation 47
    4.4.1 Controller Responses 47
  4.5 Control of Array Geometries 51
    4.5.1 String of Pearls Control 52
    4.5.2 Circular Array Control 57
    4.5.3 Y-shaped Array Control 61
  4.6 Control Summary 66

5. SYSTEM SIMULATION AND EVALUATION OF ARRAY GEOMETRIES 68
  5.1 Imaging Simulation 68
  5.2 String of Pearls 72
    5.2.1 Optimal String of Pearls Configuration 72
    5.2.2 Non-Optimal String of Pearls Configuration 75
  5.3 Circular Array 77
    5.3.1 Optimal Circular Configuration 77
    5.3.2 Non-Optimal Circular Configuration 80
  5.4 Y-Shaped Array 83
    5.4.1 Optimal Y-shape Configuration 84
    5.4.2 Non-Optimal Y-shape Configuration 86
  5.5 Imaging Simulation Conclusions 89

6. CONCLUDING REMARKS 91

REFERENCES 94

LIST OF FIGURES

FIGURE Page

2.1 Schematic showing the shadow cast upon Earth as the asteroid occults a far away star. 5

2.2 Schematic showing the shadow zone (darkly shaded) and interference zone (lightly shaded). 6

2.3 Image of asteroid Itokawa (left), *courtesy of JAXA*. Its silhouette (right) based on this image. 7

2.4 Comparison of shadow patterns for an asteroid at several Fresnel numbers. 8

2.5 Schematic showing the space-based occultation system. 9

2.6 Shadow pattern as seen on observation plane for an asteroid of $F = 0.87$. 15

2.7 Data collection pattern for 20 evenly-space apertures. 16

2.8 Silhouette reconstruction for 20 evenly-spaced apertures. 17

2.9 Data collection pattern for 10 evenly-space apertures. 18

2.10 Silhouette reconstruction for 10 evenly-spaced apertures. 18

2.11 Various aperture formation geometries. 20

3.1 Inertial and rotating frames as defined in the three-body problem. . . 23

3.2 The five libration points in the three-body problem. 30

3.3 Example of a periodic halo orbit about the Sun-Earth L_2. 35

3.4 Reference halo orbit used in simulation. 39

4.1 Magnitude of state error over time with implementation of a PD controller. 48

4.2 Spacecraft motion in the *yz*-plane over time with implementation of a PD controller. 48

4.3 Magnitude of state error over time with implementation of a LQR controller. 49

4.4 Spacecraft motion in the yz-plane over time with implementation of a LQR controller. 50

4.5 Formation motion of string of pearls array relative to the reference halo orbit using PD control. 52

4.6 Formation motion of string of pearls array relative to the reference halo orbit using LQR control. 53

4.7 Position error for each of the 21 apertures in the string of pearls formation using PD control (top) and LQR control (bottom). 54

4.8 Control time history for each of the 21 apertures in the string of pearls formation using PD control (top) and LQR control (bottom). 56

4.9 Formation motion of circular array relative to the reference halo orbit using PD control. 58

4.10 Formation motion of circular array relative to the reference halo orbit using LQR control. 58

4.11 Position error for each of the 21 apertures in the circular formation using PD control (top) and LQR control (bottom). 60

4.12 Control time history for each of the 21 apertures in the circular formation using PD control (top) and LQR control (bottom). 61

4.13 Formation motion of Y-shaped array relative to the reference halo orbit using PD control. 62

4.14 Formation motion of the Y-shaped array relative to the reference halo orbit using LQR control. 63

4.15 Position error for each of the 21 apertures in the Y-shaped formation using PD control (top) and LQR control (bottom). 64

4.16 Control time history for each of the 21 apertures in the Y-shaped formation using PD control (top) and LQR control (bottom). 65

5.1 Desired silhouette of asteroid Itokawa. 69

5.2 Shadow pattern of asteroid Itokawa at the observation plane for a Fresnel number of 0.87. 70

5.3 Optimal string of pearls array with 21 evenly-spaced apertures. . . . 73

FIGURE Page

5.4 Sensor data swept out by optimal string of pearls array. 74

5.5 Reconstructed silhouette from an optimal string of pearls array. . . . 74

5.6 Non-optimal string of pearls array with 21 evenly-spaced apertures. Shadow motion is at 30 degrees relative to the formation. 75

5.7 Sensor data swept out by non-optimal string of pearls array. 76

5.8 Reconstructed silhouette from a non-optimal string of pearls array. . 76

5.9 Optimal circular array with 21 evenly-spaced apertures. 78

5.10 Sensor data swept out by optimal circular array. 79

5.11 Reconstructed silhouette from an optimal circular array. 79

5.12 Non-optimal circular array with 21 evenly-spaced apertures. 81

5.13 Sensor data swept out by non-optimal circular array. 82

5.14 Reconstructed silhouette from a non-optimal circular array. 82

5.15 Optimal Y-shaped array with 22 evenly-spaced apertures. 84

5.16 Sensor data swept out by optimal Y-shaped array. 85

5.17 Reconstructed silhouette from an optimal Y-shaped array. 86

5.18 Non-optimal Y-shaped array with 22 evenly-spaced apertures. 87

5.19 Sensor data swept out by non-optimal Y-shaped array. 88

5.20 Reconstructed silhouette from a non-optimal Y-shaped array. 88

LIST OF TABLES

TABLE Page

3.1 Mass parameters for various systems. 25

3.2 Libration point locations for Sun-Earth system. 32

3.3 Corrected initial conditions for the reference halo orbit. 40

5.1 Parameters used in silhouette reconstruction algorithms. 71

NOMENCLATURE

Latin Letters

a	nominal radius of occulter
$A(t)$	linear, time-varying matrix of state variations in CR3BP
B	control matrix in LQR control
$B(\lambda, \underline{\theta})$	spectral radiance
C_j	Jacobi's constant
E	Fresnel integral
F	Fresnel number
G	gravitational constant
I	light intensity
$I_{n\times n}$	$n \times n$ identity matrix
J	cost function in LQR control
$K(t)$	optimal gain in LQR control
K_d	derivative gain in PID control
K_i	integral gain in PID control
K_p	proportional gain in PID control
l^*	characteristic length
L	Lagrangian
L_j	libration point j
m	mass of spacecraft in CR3BP
m^*	characteristic mass
M_1	mass of larger primary body
M_2	mass of smaller primary body

N_{sat}	total number of apertures in a formation
N_{worst}	number of useful apertures in a worst case configuration
P_1	larger primary body in CR3BP
P_2	smaller primary body in CR3BP
P_3	spacecraft in CR3BP
P_e	potential energy
Q	weighting matrix associated with state in LQR control
r_1	position vector from larger primary to spacecraft in synodic frame
r_2	position vector from smaller primary to spacecraft in synodic frame
R	weighting matrix associated with control in LQR control
$S(t)$	solution of matrix differential Riccati equation in LQR control
t	non-dimensional time
t_f	final time
t^*	characteristic time
T	period of orbit
T_e	kinetic energy
$u(t)$	applied control vector
U	complex field amplitude
U^*	pseudo-potential function in CR3BP
U^*_j	partial derivative of U with respect to j
U^*_{kl}	partial derivative of U with respect to k and l
W	shadow width
(x, y, z)	spacecraft position in synodic frame
(x_{eq}, y_{eq}, z_{eq})	location of a libration point in synodic frame
$(\dot{x}, \dot{y}, \dot{z})$	spacecraft velocity in synodic frame

$(\ddot{x}, \ddot{y}, \ddot{z})$	spacecraft acceleration in synodic frame
x_1	non-dimensional location of P_1 along $\hat{x}$-axis
x_2	non-dimensional location of P_2 along $\hat{x}$-axis
$\underline{x}$	coordinates on the object plane
(X, Y, Z)	spacecraft position in inertial frame
$(\dot{X}, \dot{Y}, \dot{Z})$	spacecraft velocity in inertial frame
$(\ddot{X}, \ddot{Y}, \ddot{Z})$	spacecraft acceleration in inertial frame
$\bar{X}_{ref}(t)$	reference trajectory in CR3BP
$\underline{X}$	coordinates on the observation plane
z	distance from occulter object to observer

Greek Letters

γ	domain where $\Gamma = 0$
Γ	silhouette function
$\delta\bar{X}(t)$	vector of state variations relative to a reference trajectory in the synodic frame
$\delta\dot{\bar{X}}(t)$	rate of change in state variations
θ	angle between synodic and inertial frame
$\underline{\theta}$	view angle
$\dot{\theta}$	angular rate of synodic frame relative to inertial frame
λ	center band wavelength of light
λ	eigenvalues associated with linearized equations of motion in CR3BP
λ	costate in derivation of LQR control
μ	non-dimensional mass parameter
ρ	data coverage ratio

$\Phi(t, t_0)$	state transition matrix in CR3BP

Acronyms

CR3BP	circular restricted three-body problem
LQR	linear quadratic regulator
NEA	near-Earth asteroid
PID	proportional integral derivative
SNR	signal-to-noise ratio

1. INTRODUCTION

This work examines control strategies for and optical performance of a formation of telescope-baring spacecraft, located near the Sun-Earth L_2 libration point. The formation is designed to detect and characterize small but potentially dangerous near Earth asteroids (NEAs) using an advanced technique of stellar occultation.

1.1 Background

Observational tasks such as inspection of resident space objects, imaging of exoplanets and characterization of potentially hazardous near Earth asteroids (NEAs) require extremely fine angular resolution. Because of the Rayleigh relation [1] between resolution and aperture size, conventional monolithic telescopes meeting the resolution requirements must be very large. Such facilities would be extremely costly to build on the ground and nearly impossible to deploy in space. This motivated such programs as the Space Interferometry Mission (SIM) and the Terrestrial Planet Finder (TPF) Interferometer to consider systems composed of arrays of spatially distributed, modestly-sized apertures [2, 3]. These systems process the information gathered by the several apertures to determine an image or object profile. The apertures may be structurally connected or reside in free-flying spacecraft. This work is concerned with the latter approach.

A conventional way to generate images from the measurements of a formation of distributed apertures is amplitude interferometry [4]. In this approach, each light collector transmits its beam to combiner units that measure the amplitude and phase of the mutual coherence associated with each pair of apertures. The underlying image is attained by Fourier transformation in accordance with the Van Cittert-Zernike theorem [5]. For ground systems, complex adaptive optics equipment is needed to remove the phase scintillations due to turbulent atmospheric inhomogenieties. In a space-based system this complexity is removed, but precise control is needed, not only for the light-collecting apertures, but also for their numerous combiner units. This gives rise to intractable formation maneuver difficulties.

The above complexities are removed, however, for a species of astronomy known as flux collector ("light bucket") astronomy [6]. Here, each telescope is not used as an image forming device, but is instead designed to record the arrival of photons collected by its aperture. This approach entails no combiner units. In the intensity correlation interferometry technique, the photon arrival times are correlated for each aperture pair and a phase retrieval algorithm is used to compute the image. It has been shown that this is insensitive to both phase and amplitude scintillations due to atmospheric turbulence [7]. A simpler approach, stellar occultation, determines the silhouette of an object that occults a star by observing the light intensities at each aperture. Provided that the aperture field-of-view is wide enough to encompass the focal plane jitter, this method is also insensitive to phase scintillations. A convenient and very popular technique reconstructs the profile of main-belt asteroids by using an array of observers who simply record the times at which the occulted star disappears and when it reappears [8]. However, this is practical only when the asteroid casts a sharp shadow. We are interested in characterizing NEAs in the 140 to 40 meter diameter range, of which only approximately 1 percent have been identified [9]. While too small and distant to cast sharp shadows, these asteroids are still large enough to cause severe damage on Earth impact. Recently, Hyland and Altwaijry [10] developed a system design that determines the sharp silhouette of an object occulting a star even when the shadow is heavily diffracted. An array of small telescopes records the time histories of the light intensity patterns of the shadow, then algorithms devised by Hyland and Trahan [11] are used to construct a sharp silhouette. Besides size and shape data, the technique also yields much orbital parameter data: approximate distance, exact position and apparent velocity.

A plan for a Low-Earth-Orbit (LEO) flight test to demonstrate the stellar occultation technology was studied by the California Institute of Technology's Jet Propulsion Laboratory and is reported in [12]. In these studies the operational requirements for the formation control were formulated. The longer term plan is to assemble a fully operational system to operate over a $>$ 10 year mission. To provide 24-7 observing time, the system should be space-based. Also to minimize the influence of gravity gradients on the control of the array geometry, it is desired to place the telescope array in a halo orbit around the Sun-Earth L2 point. The present work evaluates formation control that meets the imaging quality requirements in the environment of a circular restricted three-body problem (CR3BP) dynamical system. Multiple geometries are then evaluated for their performance in reconstructing silhouettes using only those measurements taken by apertures in the array.

1.2 Objectives and Organization of the Study

The current investigation involves control strategies for formations of telescope-bearing spacecraft designed to characterize NEAs and other small, distant objects by means of stellar occultation. This work uses previously developed models for estimating the statistics and typical parameters of stellar occultations and the occulting NEAs to formulate control requirements on the motions of the spacecraft formation components. In addition, this work furthers developement of system requirements pertaining to data coverage and aperture positioning. Notional image reconstruction and formation motion are simulated for varying mission parameters, including formation geometry and number of apertures.

The study is organized as follows. In Chapter 2, the formulation of the occultation imaging method is reviewed and the requirements on the formation size, geometry and motion to secure adequate characterization accuracy are reviewed. Chapter 3 discusses the relevant dynamical equations for the CR3BP design environment. In Chapter 4, control methods for formations of spacecraft are designed and implemented for formations moving in halo orbits around Sun-Earth system libration points in the CR3BP. In Chapter 5, the stellar occultation system is simulated and three various candidate geometries are evaluated based on their ability to reconstruct an asteroid silhouette. Chapter 6 offers concluding remarks and suggestions for future research directions.

2. OCCULTATION IMAGING METHOD

Stellar occultation is a widely-used method to characterize objects such as near-Earth asteroids, moons, and minor planets. This method is easily employed by both amateur and professional astronomers. Many Kuiper belt objects and moons have been successfully characterized using this method [13, 14, 15, 16, 17]. The conventional use of this method employs a set of ground observers to note the time and duration that a star's light blinks out from an object passing in front of it. Examination of the occultation event by several observers in different locations enables the ground track of the occulting object to be plotted and its size to be estimated. Figure 2.1 shows a schematic of a stellar occultation event.

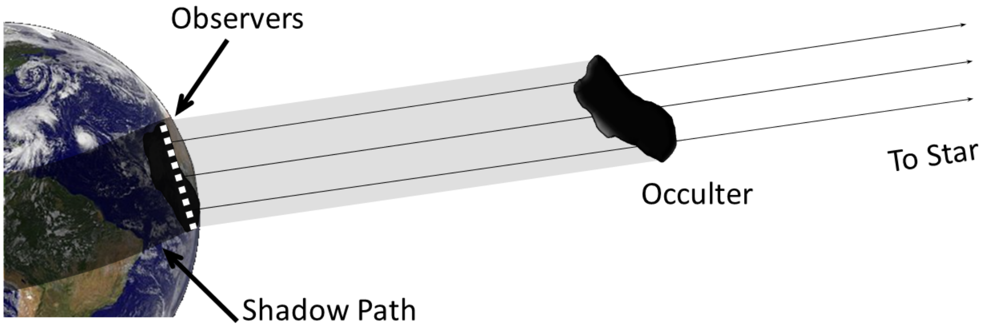

Figure 2.1: Schematic showing the shadow cast upon Earth as the asteroid occults a far away star.

This conventional stellar occultation method has been used to successfully characterize space-fairing objects for many years. However, the major limitation to this method is that it assumes the occulting object is large enough or close enough to cast a sharp shadow. In reality, the edge of a shadow is subject to diffraction and no clear shadow exists far away from the object. For instance, smaller asteroids that do not reside in the main asteroid belt create shadow patterns that are heavily diffracted, making identification and characterization of them difficult. The Fresnel number is a metric commonly used to characterize the level of diffraction that a shadow exhibits. The Fresnel number is defined as

$$F = \frac{a^2}{z\lambda} \tag{2.1}$$

where a is the nominal radius of the object, z is the distance between the object and the observer, and λ is the center band wavelength of light considered. A schematic of the various shadow regions is illustrated in Figure 2.2.

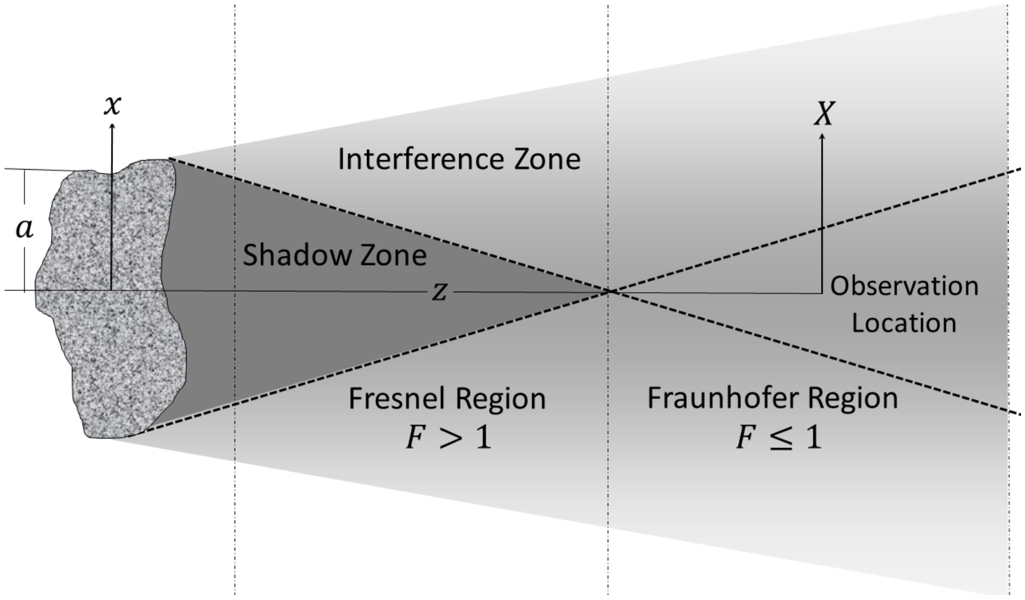

Figure 2.2: Schematic showing the shadow zone (darkly shaded) and interference zone (lightly shaded).

As shown in Figure 2.2 and accounted for in calculation of the Fresnel number, the light field as seen from an observer down range of an occulting object is dependent on the distance between the observer and the object, as well the nominal size of the object. A dark, sharp shadow exists only in the region where the Fresnel number is much greater than unity, called the Fresnel region. For the smaller near-Earth asteroids considered in this work, the Fresnel number is typically much less than unity and a sharp shadow does not exist at the observer's location. This region where $F < 1$ is known as the Fraunhofer region. In this region, shadow patterns are observed as interference patterns. To illustrate this point, consider the asteroid Itokawa, whose silhouette is shown in Figure 2.3.

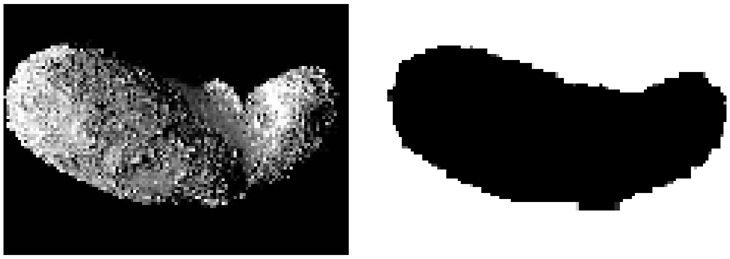

Figure 2.3: Image of asteroid Itokawa (left), *courtesy of JAXA*. Its silhouette (right) based on this image.

The image on the left of Figure 2.3 was taken by the Japanese Aerospace Exploration Agency (JAXA) during the Hayabusa mission [18]. The silhouette on the right was created based on this image. By varying the asteroid's distance from the observer, the shadow pattern at the observation plane changes. For various Fresenel numbers, the resulting shadow patterns are shown in Figure 2.4.

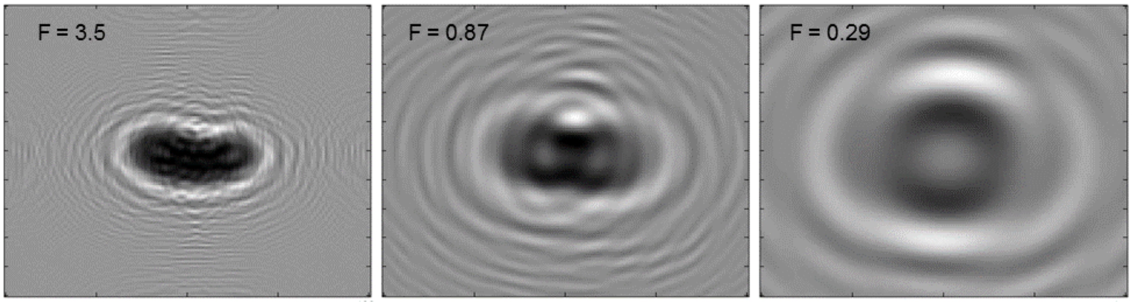

Figure 2.4: Comparison of shadow patterns for an asteroid at several Fresnel numbers.

As shown in Figure 2.4, for asteroids residing in regions where the Fresnel number is less than unity, it is unlikely that the shadow pattern can be used to visually characterize the shape of the occulter. As a result, asteroids residing in the Fraunhofer region must be analyzed through an alternative process, which analyzes the shadow patterns through an intensity mapping technique.

Most efforts in the field focus on retrieving a nominal radius of the occulting object [19] and recent work has expanded circular estimates to include ellipses [20]. However, it is desired here to retrieve the shape of an occulter with greater fidelty than a single characteristic radius or geometric shape. Hyland and Altwaijry [10] developed such an occultation system for space-based operations, which is capable of characterizing asteroids residing in the Fraunhofer region using the theory of shadow diffraction and phase retrieval technology. It was shown that this technique provides an approximate distance, lateral velocity, position, time, size, and shape of a simulated asteroid using a circular array of apertures. Hyland [21] expanded on this work to include initial estimates of the signal-to-noise ratio (SNR) as well as the expected frequency of observation opportunities. Trahan [11, 22] expanded the efficiency and convergence of the technique by developing a specialized phase retrieval algorithm. Development of the aperture formation and how it relates to the algorithm's performance were left for future work by Trahan and is examined in the current study.

This chapter focuses on design of the aperture formation and how it relates to the ability of the novel stellar occultation system to identify and characterize near-Earth asteroids residing in the Fraunhofer region. The following sections detail the method of resolving asteroid silhouettes, as well as development of system requirements that are used in simulation of formation geometry and dynamics in later chapters.

2.1 Method of Resolving Asteroid Silhouettes

The novel asteroid characterization technique considered here uses light intensity measurements over time and the Huygens-Fresnel principle to transform a highly diffracted shadow pattern into a sharp silhouette. Figure 2.5 depicts the space-based stellar occultation system under consideration.

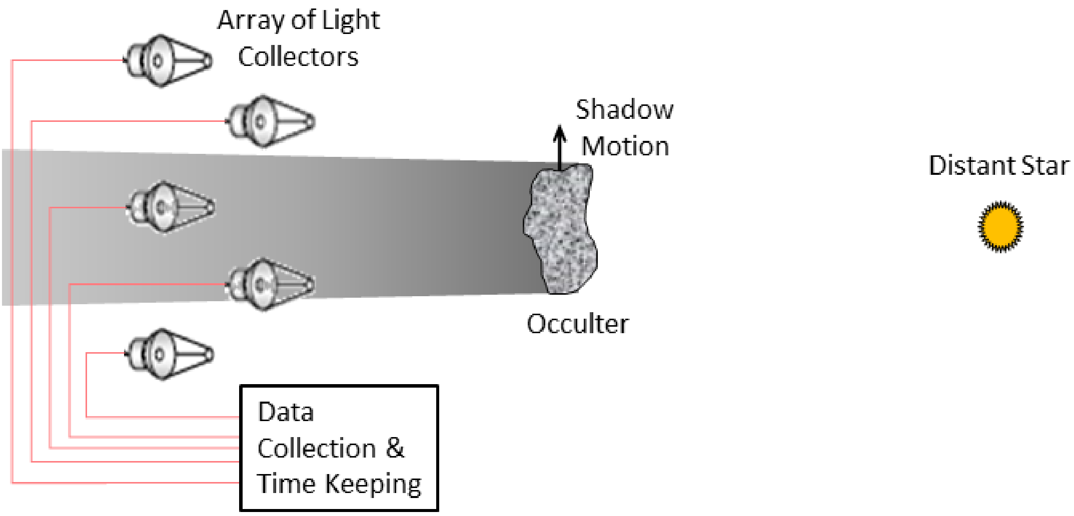

Figure 2.5: Schematic showing the space-based occultation system.

Consider the object plane with coordinates $\underline{x} = (x, y)$ and an observation plane in the Fraunhofer region with coordinates $\underline{X} = (X, Y)$. The planes are parallel and separated by distance z. When scaled by the separation distance, the object plane can be described by the view angle $\underline{\theta} = \underline{x}/z = (\theta_x, \theta_y)$ and the observation plane can be represented by $\underline{u} = \underline{X}/z = (u, v)$. Assuming that the star is a point source and the occulter lies within the object plane, the complex field at the object plane is defined by the shape of the occulter. This shape is characterized by the silhouette function defined as

$$\Gamma(\underline{\theta}) = \begin{cases} 0, & \text{if } \underline{\theta} \text{ is inside asteroid profile} \\ 1, & \text{otherwise} \end{cases} \tag{2.2}$$

The purpose of stellar occultation methods is to determine this silhouette function. Algorithms developed to estimate the shape of the occulting object (silhouette function) based on the intensity distribution (shadow pattern) at the observation plane are detailed in the following sections.

2.1.1 Data Collection

Refer to the space-based stellar occultation system in Figure 2.5. An array of light-collecting apertures form the observation plane. At each aperture, the light intensity is recorded over time and used to form the shadow pattern. The shadow pattern is simply the pattern of light intensity that would be recorded on a plane moving with the NEA's shadow. Normalizing the light intensity with respect to the unocculted star, the magnitude of the complex field at the observation plane is known,

$$I(x) = |U(\underline{x})|^2. \tag{2.3}$$

Treating the star as a point source, the field amplitude is given by,

$$U(\underline{x}) = U_{ps}(\lambda, z, \underline{x}) = \frac{z}{\lambda} \int \left[\Gamma(\underline{\theta}) \exp\!\left(\frac{zi\pi}{\lambda} \underline{\theta} \cdot \underline{\theta} \right) \right] \exp\!\left(\frac{-2i\pi}{\lambda} \underline{x} \cdot \underline{\theta} \right) d^2\theta. \tag{2.4}$$

The quantity of interest is the silhouette function, defined above in equation 2.2. Treating the light source as an extended incoherent source, the total shadow pattern is given by the convolution integral

$$I_{total}(\underline{x}) = \int_{\lambda-\Delta\lambda/2}^{\lambda+\Delta\lambda/2} d\lambda \int B(\lambda,\underline{\theta}) \Big| U_{ps}(\underline{x} - z\underline{\theta}) \Big|^2 d^2\theta \tag{2.5}$$

where $B(\lambda, \underline{\theta})$ is the normalized spectral radiance, $\Delta\lambda$ is the band-pass width of a gray band-limited filter, λ is the center band wavelength, and $\underline{\theta}$ is the look angle position. Given the intensity pattern at the observation plane, equations 2.4 and 2.5 are used to compute the silhouette function via processes resembling phase retrieval algorithms.

If we assume that the spectral radiance of the filtered source is slowly varying over the filter wave band, then equation 2.5 can be approximated as

$$I_{total}(\underline{x}) \approx \Delta\lambda \int B(\lambda,\underline{\theta}) \Big| U_{ps}(\lambda, \underline{x} - z\underline{\theta}) \Big|^2 d^2\theta. \tag{2.6}$$

A Fourier transform pair is defined such that

$$F_{\underline{u}}\Big[f(\underline{x})\Big] = \int_{-\infty}^{\infty} f(\underline{x}) \exp(2i\pi \underline{u} \cdot \underline{x}) d^2x \tag{2.7}$$

$$F_{\underline{x}}^{-1}\Big[F(\underline{u})\Big] = \int_{-\infty}^{\infty} F(\underline{u}) \exp(-2i\pi \underline{u} \cdot \underline{x}) d^2u. \tag{2.8}$$

Taking the Fourier transform of both sides of equation 2.6 and applying the convolution theorem,

$$F_{\underline{u}}\Big[I_{total}(\underline{x})\Big] = \frac{\Delta\lambda}{z^2} F_{\underline{u}}\Big[B(\lambda,\underline{\theta})\Big] F_{\underline{u}}\Big[\Big|U_{ps}(\lambda,\underline{x})\Big|^2\Big]. \tag{2.9}$$

Solving for $\left|U_{ps}(\lambda, \underline{x})\right|$ in equation 2.9 yields

$$\left|U_{ps}(\lambda, \underline{x})\right| = \sqrt{F_{\underline{x}}^{-1}\Big[\frac{z^2}{\Delta\lambda}\frac{F_{\underline{u}}[I_{total}(\underline{x})]}{F_{\underline{u}}[B(\lambda, \underline{\theta})]}\Big]}. \tag{2.10}$$

Inverting the relationship in equation 2.4 for $\Gamma(\underline{\theta})$ gives

$$\Gamma(\underline{\theta}) = \frac{1}{\lambda z}\exp\Big(\frac{zi\pi}{\lambda}\underline{\theta}\cdot\underline{\theta}\Big)\int [U_{ps}(\lambda, \underline{x})]\exp\Big(\frac{2i\pi}{\lambda}\underline{x}\cdot\underline{\theta}\Big)d^2x \tag{2.11}$$

For most cases, $F_{\underline{u}}[B(\lambda, \underline{\theta})]$ is approximateley Gaussian so that the denominator of equation 2.10 has no zeros. Equation 2.10 gives the magnitude of the field amplitude as a function of the measured light intensity. When combined with the image-domain constraints on the silhouette function (pixels are either zero or unity), this information enables calculation of the complete field amplitude (magnitude and phase) with use of a phase retrieval algorithm. The phase retrieval algorithm is detailed in the following section. Equation 2.11 shows that the silhouette function is the inverse Fourier transform of $U_{ps}(\lambda, \underline{x})$.

2.1.2 Phase Retrieval Algorithm

Equation 2.4 is the standard Fresnel diffraction equation and describes the wave field at distance z from the occulting object. Its magnitude is the known quantity when measuring the intensity distribution at the observation array. Trahan [11] showed that the light intensity can be represented as

$$I(\underline{u}) = \left|\frac{z}{\lambda}\int_{\mathbb{R}^2}\exp\Big(\frac{zi\pi}{\lambda}(\underline{u}-\underline{\theta})^2\Big)d\underline{\theta} - \frac{z}{\lambda}\int_{\gamma}\exp\Big(\frac{zi\pi}{\lambda}(\underline{u}-\underline{\theta})^2\Big)d\underline{\theta}\right|^2 \tag{2.12}$$

where γ is the domain where $\Gamma(\underline{\theta}) = 0$. The problem then simplifies to describing the region γ such that its shape can be estimated. Treating γ as a grid of binary values, the second integral of equation 2.12 becomes a summation of continuous integrals over the elements

$$I(\underline{u}) = \left|\frac{z}{\lambda}\int_{\mathbb{R}^2} \exp\Bigl(\frac{zi\pi}{\lambda}(\underline{u}-\underline{\theta})^2\Bigr)d\underline{\theta} - \frac{z}{\lambda}\sum(1-\Gamma_{i,j})\int_{A_{i,j}} \exp\Bigl(\frac{zi\pi}{\lambda}(\underline{u}-\underline{\theta})^2\Bigr)d\underline{\theta}\right|^2 \quad (2.13)$$

where $A_{i,j}$ represents the grid domain. Using the complex form of the Fresnel integral,

$$E(x) = \int_0^x \exp\Bigl(\frac{t^2 i\pi}{2}\Bigr)dt \quad (2.14)$$

equation 2.13 expands to form

$$\begin{aligned} I(\underline{u}) = \Biggl| i - \frac{1}{2}\sum(1-\Gamma_{i,j}) \\ &\times \left(E\left[\sqrt{\frac{2z}{\lambda}}(\theta_{x,i}+\Delta x - u)\right] - E\left[\sqrt{\frac{2z}{\lambda}}(\theta_{x,i} - u)\right]\right) \\ &\times \left(E\left[\sqrt{\frac{2z}{\lambda}}(\theta_{y,i}+\Delta y - v)\right] - E\left[\sqrt{\frac{2z}{\lambda}}(\theta_{y,i} - v)\right]\right)\Biggr|^2. \end{aligned} \quad (2.15)$$

A simple raster scan method is used to estimate the γ region. After making a guess for $\Gamma_{i,j}$ (either zero or unity at each pixel), the field's squared magnitude is calculated using equation 2.15 and compared to the actual measured intensity using an error parameter. Each grid element is changed to see if the resulting intensity error improves. When the two shadow patterns match within a specified tolerance, an estimate for γ, and thus the silhouette function Γ, has been found.

2.1.3 Asteroid Characterization

Much information can be learned about the occulting object from the estimated shadow function and resulting silhouette without a priori knowlege about it. The interference striations in the shadow function, as well as its overall width in the observation plane, give an estimate of the Fresnel number F. The silhouette gives a size a, and this used in combination with F gives an estimated distance to the asteroid z. The apparent angular velocity and lateral direction of the NEA can also be estimated when processing the shadow pattern, based on the specific geometry of the array and mutual coherence of paired apertures. Such parameters can be utilized for follow up tracking of the NEA by optics or radar. The radiance of the NEA can be measured just after occultation from the reflected sunlight. When combined with the size a, this information can establish the albedo of the asteroid. And finally, the detailed shape of the silhouette gives information about the internal structure of the asteroid. For example, a smooth and rounded shape would tend to be a more compact structure; while a bulbous, conglomerate shape would indicate a rubble pile.

2.2 Data Coverage and Aperture Positioning

Given that the goal of this method is to characterize the silhouette of the occulting asteroid using the shadow pattern, it is imperative that the formation be designed such that there is adequate coverage of the observation plane. The end-to-end extent of the array must be at least as large as the width of the shadow region W pertaining to the center band wavelength λ,

$$W = 2\left[a + \frac{\bar{\lambda} z}{a}\right]. \tag{2.16}$$

The Fresnel integral fluctuations are strongest near the edges of the object. When far from the shadow, these fluctuations contain little information about the silhouette. Thus the array need not be much larger than this width. The next step is deciding on the desired number of pixels on a side that the final silhouette will have. More pixels enable the silhouette to have better resolution and finer detail, but requires a greater number of apertures covering the observation plane. A typical number is 20 pixels in length. This silhouette resolution will be used in all further analysis in this study.

The previous sections used knowledge of a shadow pattern of continuous data. In reality the shadow pattern is only known at specified positions given by the aperture locations in the array at the time of occultation. Because the asteroid's shadow is moving at high velocity relative to the formation, each aperture collects intensity measurements in a straight line across the shadow pattern. Think of the apertures as prongs of a rake, sweeping out lines of data across the shadow pattern as a rake would sweep out lines in the sand. Consider the shadow pattern shown in Figure 2.6, which represents an asteroid with the true silhouette shown in Figure 2.3 and located 1 AU away from the observer. The asteroid Itokawa was chosen so that this work could build upon the previous work of Trahan [23]; however, all images produced in this thesis are of the author's own simulation, unless otherwise noted.

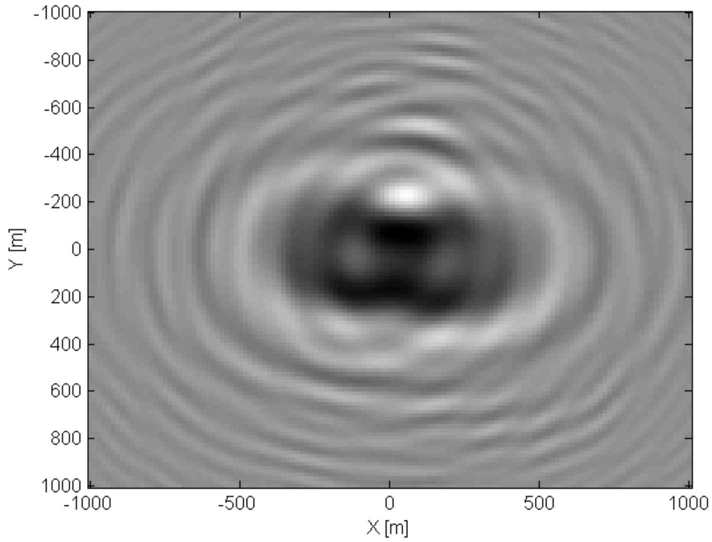

Figure 2.6: Shadow pattern as seen on observation plane for an asteroid of $F = 0.87$.

As shown, the asteroid's shadow pattern is heavily diffracted at the observation plane, with a Fresnel number of 0.87. For a string of pearls array of 20 evenly-spaced apertures, approximately 80 meters apart, the data collection pattern is shown in Figure 2.7.

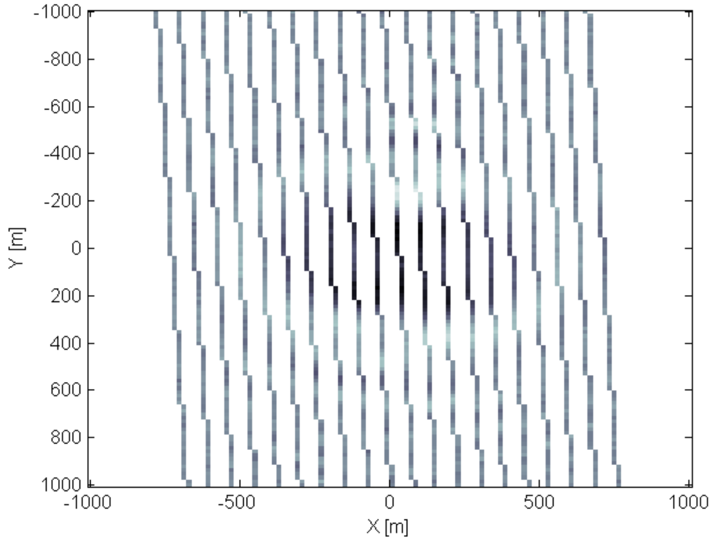

Figure 2.7: Data collection pattern for 20 evenly-space apertures.

Here, the lines of measurement swept out by each aperture are shown. The white regions denote an absence of data. The resulting reconstructed silhouette is shown in Figure 2.8. Perfect silhouette reconstruction is achieved after 3.5 iterations. This implies that sufficient data was collected from the shadow pattern. In other words, an appropriate number of apertures was used in the array.

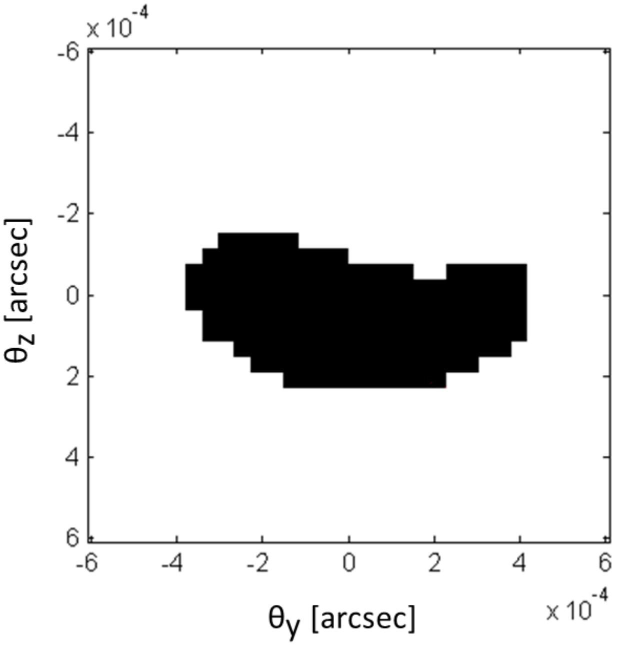

Figure 2.8: Silhouette reconstruction for 20 evenly-spaced apertures.

Decreasing the string of pearls formation to 10 evenly-spaced apertures, approximately 150 meters apart, Figures 2.9 and 2.10 show the lines of measurement swept out by the array and the resulting silhouette estimate.

The above silhouette is the result of 10 iterations, during which convergence was not met. This shows that the process begins to break down if enough measurements (apertures) are not used. The general shape of the asteroid is evident with several extraneous pixels around the exterior of the asteroid and many holes on the interior of the asteroid. Visual manipulation of the silhouette would help the algorithm to converge.

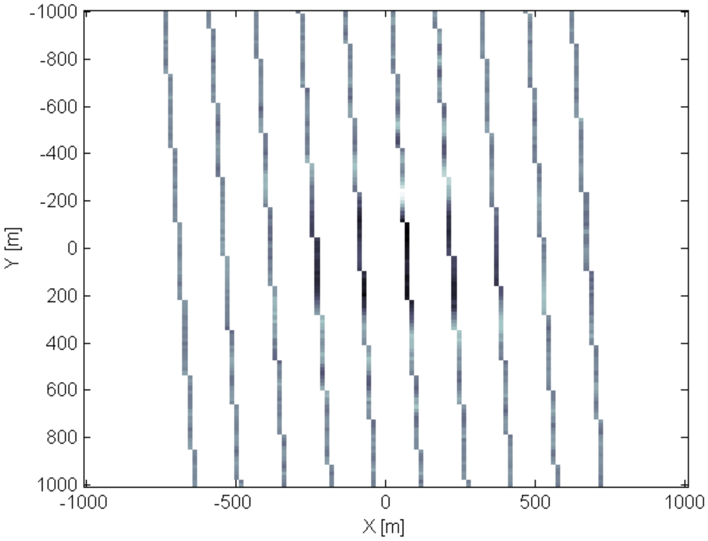

Figure 2.9: Data collection pattern for 10 evenly-space apertures.

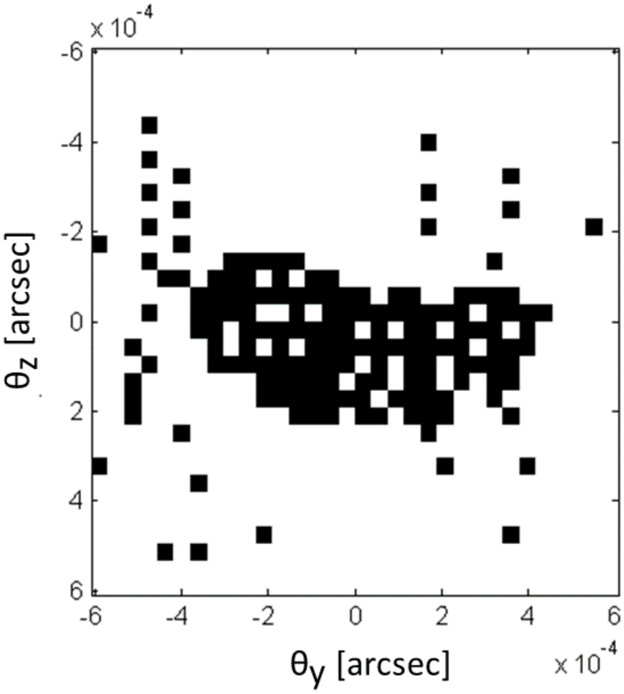

Figure 2.10: Silhouette reconstruction for 10 evenly-spaced apertures.

As illustrated by this example, a sufficient number of apertures is necessary for successful silhouette reconstruction. To quantify the quality of data coverage, a parameter was defined by Trahan [23]

$$\rho = \frac{\text{No. of Measurements}}{\text{No. of Pixels on a Side in Silhouette}}. \tag{2.17}$$

This parameter ρ was used to establish a theoretical minimum number of measurements for the system. The number of constraints on the system should be greater than the number of unknowns. This means that the number of measurements taken by the formation must be greater than the number of pixels across the silhouette. Analyzing a string of pearls array about the Earth, it was determined that the threshold of data collection for reliable silhouette recovery requires approximately $\rho = 2$. However, the present study indicates that this may be too stringent and a value of $\rho \approx 1$ can suffice. Thus, the number of measurements spaced along the cross track direction of shadow motion should be approximately equal to the number of pixels on a side of the desired silhouette. This is clearly shown to be the case for the example given above where 20 evenly-spaced apertures successfully resolved a silhouette of 20 pixels in Figure 2.8. Thus this relationship was used in determining the minimum number of apertures in the formations of the current study.

There are an endless number of array geometries that can be used in this space-based occultation system. Hyland [10] examanied a circular formation, while Trahan [23] examined a string of pearls in Low Earth Orbit. Another geometry examined in this paper is a Y-shaped array. Each of these geometries is depicted in Figure 2.11.

Figure 2.11: Various aperture formation geometries.

For a desired resolution at the observation plane, each geometry will have a different required number of apertures. This is due to the fact that sufficiently many samples of the shadow time history must be taken in the cross-track direction (perpendicular to the apparent motion of the shadow) to reveal enough useful information for asteroid characterization. Thus, while some geometries may provide for multiple cross-track directions (e.g. circular versus string of pearls), only those apertures collecting light in the cross-track direction, not the total number of apertures in the formation, will be useful for characterizing a specific asteroid. Consider the following example.

For a given requirement of 20 pixels along the desired silhouette, a minimum of 20 apertures are required in the cross-track direction. Assuming the best case scenarios, both the string of pearls and the circular array require 20 apertures. However, the string of pearls offers this resolution in one direction, while the circular array offers 360 degrees within the viewing plane. This best case scenario also assumes that none of the apertures in the circular array cover redundant measurements. In other words, that no two apertures are aligned such that they measure the same intensity pattern. While this can be useful in determining the direction and speed of shadow movement, as well as increasing the SNR of intensity measurements, it is not helpful in resolving the silhouette. Assuming the worst case scenario, half of the circular array's apertures would become redundant, with only 10 apertures taking useful measurements. Thus if preparing for the worst case configuration, the circular array would require 40 apertures. The Y-shaped formation may offer a compromise between the first two geometries by minimizing the number of apertures required and still offering multiple directions of coverage. The requirements for each of the three geometries are examined in Chapter 5.

3. THREE-BODY PROBLEM DYNAMICS

Orbits about libration points are ideal locations for imaging arrays. The Sun-Earth L_2 point is chosen as the location for the occultation array in this study for several reasons. Firstly, it is a relatively low energy location and requires little fuel to travel to. Secondly, it exhibits lower gravity gradients than Low Earth Orbit and thus should require less control to keep the formation intact. Thirdly, it is a relatively quiet environment optically in that radiation from the Earth will not interfere with the measurements taken there. Lastly, if a halo orbit is used, there can be uninterrupted communications with the Earth, while never experiencing blocked fields of view from the Earth or Sun when imaging. For these reasons, a halo orbit about the Sun-Earth L_2 point is chosen as the desired location.

Because the occultation method used here requires specific formations to be maintained, the dynamics associated with the formation under the influence of both the Sun and Earth need to be addressed. The focus of this chapter is spacecraft moving under the influence of multiple gravitational bodies. The circular restricted three-body problem (CR3BP) is the mathematical model used to describe the spacecraft's motion. First the equations of motion for the CR3BP are developed and explained. Properties associated with the differential equations are explored, such as constants of motion and particular solutions to the equations. From these developments, the five libration points of the system are found. The problem is simplified by linearizing the equations of motion about the collinear libration points, and finally, orbits unique to the libration points are examined–specifically periodic halo orbits. The chapter closes with derivation of a targeting method which is used to solve for these orbits.

3.1 Circular Restricted Three-Body Problem

Spacecraft moving under the influence of multiple gravitational bodies, such as the Earth-Moon or Sun-Earth systems can be modeled using the circular restricted three-body problem (CR3BP). Consider the motion of a particle moving in the vicinity of two larger primary bodies, such that the mass of the particle does not affect motion of the other two bodies. The two primaries revolve about their common center of mass, or barycenter, in Keplarian orbits. This system is termed the restricted three-body problem. If it is also assumed that the two primaries move in circular orbits, the problem is referred to as the circular restricted three-body problem. The geometry of the three-body problem appears in Figure 3.1.

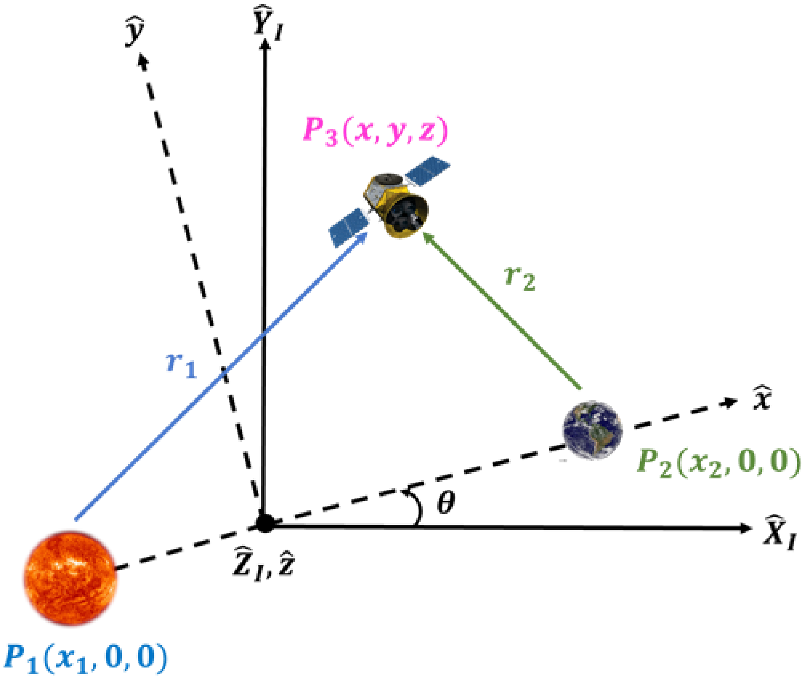

Figure 3.1: Inertial and rotating frames as defined in the three-body problem.

From Figure 3.1, the primary bodies are given by P_1 and P_2 and the spacecraft is given by P_3. The more massive of the two primary bodies is taken to be P_1. The inertial frame ($\hat{X}_I$-$\hat{Y}_I$-$\hat{Z}_I$) is centered on the barycenter of the two primaries, with the $\hat{Z}_I$-axis normal to the orbital plane of motion. The rotating frame ($\hat{x}$-$\hat{y}$-$\hat{z}$) is also centered on the barycenter of the two primaries, with the $\hat{x}$-axis directed toward P_2 and the $\hat{z}$-axis normal to the orbital plane of motion. The $\hat{y}$-axis completes the right-handed triad. This synodic frame rotates with angular rate $\dot{\theta}$ with respect to the inertial frame. For the current work, the Sun is taken to be P_1 and the Earth as P_2. Each aperture in the formation will be modeled as P_3. The following developments and derivations follow references such as [24, 25, 26].

3.2 Non-dimensional Coordinates and Characteristic Values

To facilitate analysis for a variety of problems, characteristic quantities are defined such that the significant parameters of the system can be normalized. The total mass of the system primaries is used to define a characteristic mass such that

$$m^* \equiv M_1 + M_2. \tag{3.1}$$

The characteristic length is given by the average distance between the two primaries

$$l^* \equiv |x_2 - x_1|. \tag{3.2}$$

Next, the characteristic time is chosen such that

$$t^* \equiv \left(\frac{l^{*3}}{Gm^*}\right)^{1/2}. \tag{3.3}$$

Here, G is the universal gravitational constant. Using this definition, the rotation rate of the synodic frame with respect to the inertial frame becomes unity ($\dot{\theta} = 1$). These characteristic quantities are used to non-dimensionalize the system. A mass parameter is defined using the characteristic mass such that,

$$\mu = \frac{M_2}{m^*}. \tag{3.4}$$

Using the mass parameter, the non-dimensional masses of the primaries become

$$M_1 = 1 - \mu \tag{3.5}$$

$$M_2 = \mu \tag{3.6}$$

and the non-dimensional locations of the primaries become

$$x_1 = -\mu \tag{3.7}$$

$$x_2 = 1 - \mu. \tag{3.8}$$

For the Sun-Earth system, $\mu \approx 3.0034 \times 10^{-6}$. Table 3.1 gives the mass parameters for a variety of systems.

Table 3.1: Mass parameters for various systems.

System	Mass Parameter
Sun-Earth	3.0034×10^{-6}
Sun-Earth+Moon	3.0404×10^{-6}
Sun-Jupiter	9.5387×10^{-4}
Earth-Moon	1.21507×10^{-2}

3.3 Equations of Motion

Referring to Figure 3.1, a relationship exists between the inertial and rotating reference frames,

$$X = x\cos\theta - y\sin\theta \tag{3.9}$$

$$Y = x\sin\theta + y\cos\theta \tag{3.10}$$

$$Z = z \tag{3.11}$$

where all quantities are non-dimensional. Differentiation of equations 3.9, 3.10, and 3.11 with respect to time yields the following kinematic expressions,

$$\dot{X} = (\dot{x} - \dot{\theta}_y)\cos\theta - (\dot{y} + \dot{\theta}_x)\sin\theta \tag{3.12}$$

$$\dot{Y} = (\dot{x} - \dot{\theta}_y)\sin\theta + (\dot{y} - \dot{\theta}_x)\cos\theta \tag{3.13}$$

$$\dot{Z} = \dot{z} \tag{3.14}$$

where $\dot{\theta}$ is the angular rate of the rotating coordinate frame with respect to the inertial frame.

Using equations 3.12,3.13, and 3.14, the total kinetic energy of the spacecraft is given by,

$$T_e = \frac{m}{2}[\dot{X}^2 + \dot{Y}^2 + \dot{Z}^2] \tag{3.15}$$

$$= \frac{m}{2}\Big[(\dot{x} - \dot{\theta}_y)^2 + (\dot{y} + \dot{\theta}_x)^2 + (\dot{z})^2\Big] \tag{3.16}$$

where m is the mass of the spacecraft. Due to the gravitational forces on the spacecraft from P_1 and P_2, the potential energy is given by

$$P_e = -m\Big[\frac{(1-\mu)}{r_1} + \frac{\mu}{r_2}\Big] \tag{3.17}$$

where

$$r_1 = \sqrt{(x+\mu)^2 + y^2 + z^2)} \tag{3.18}$$

$$r_2 = \sqrt{(x-(1-\mu))^2 + y^2 + z^2} \tag{3.19}$$

represents the distance between the primaries P_1 and P_2 with the spacecraft P_3. Next forming the Lagrangian,

$$L = T_e + P_e \tag{3.20}$$

the equations of motion are

$$\ddot{x} - 2\dot{\theta}\dot{y} = \ddot{\theta}_y + \dot{\theta}^2 x - \frac{(1-\mu)}{r_1^3}(x+\mu) - \frac{\mu}{r_2^3}(x-(1-\mu)) \tag{3.21}$$

$$\ddot{y} + 2\dot{\theta}\dot{x} = -\ddot{\theta}_x + \dot{\theta}^2 y - \Big[\frac{(1-\mu)}{r_1^3} + \frac{\mu}{r_2^3}\Big]y \tag{3.22}$$

$$\ddot{z} = -\Big[\frac{(1-\mu)}{r_1^3} + \frac{\mu}{r_2^3}\Big]z. \tag{3.23}$$

Assuming the primaries move on circular orbits ($\ddot{\theta} = 0$), equations 3.21, 3.22, and 3.23 can be further simplified,

$$\ddot{x} - 2\dot{y} - x = -\frac{(1-\mu)(x+\mu)}{r_1^3} - \frac{\mu(x-(1-\mu))}{r_2^3} \tag{3.24}$$

$$\ddot{y} + 2\dot{x} - y = -\frac{(1-\mu)y}{r_1^3} - \frac{\mu y}{r_2^3} \tag{3.25}$$

$$\ddot{z} = -\frac{(1-\mu)z}{r_1^3} - \frac{\mu z}{r_2^3}. \tag{3.26}$$

Equations 3.24, 3.25, and 3.26 are the non-dimensional, nonlinear equations of motion that comprise the CR3BP mathematical model. Motion of the spacecraft in the CR3BP is given in terms of the rotating reference frame and relative to the barycenter of the system primaries. A closed form analytic solution to the CR3BP is not known to exist.

3.4 Pseudo-Potential and Jacobi's Constant

Given the pseudo-potential,

$$U^* = \frac{(1-\mu)}{r_1} + \frac{\mu}{r_2} + \frac{1}{2}(x^2 + y^2) \tag{3.27}$$

the differential equations of motion governing the CR3BP can be rewritten as

$$\ddot{x} = U_x^* + 2\dot{y} \tag{3.28}$$

$$\ddot{y} = U_y^* - 2\dot{x} \tag{3.29}$$

$$\ddot{z} = U_z^* \tag{3.30}$$

where U_j^* denotes $\frac{\partial U^*}{\partial j}$. Multiplying equations 3.28, 3.29, 3.30 by $\dot{x}$, $\dot{y}$, and $\dot{z}$ respectively and adding them together yields,

$$\dot{x}\ddot{x} + \dot{y}\ddot{y} + \dot{z}\ddot{z} = U_x^*\dot{x} + U_y^*\dot{y} + U_z^*\dot{z} = \frac{dU^*}{dt}. \tag{3.31}$$

Integrating equation 3.31 with respect to time yields the Jacobi integral,

$$\dot{x}^2 + \dot{y}^2 + \dot{z}^2 = 2U^* - C_j \tag{3.32}$$

where the integration constant, C_j, is known as the Jacobi Constant. The energy-like Jacobi Constant allows significant insight into the CR3BP and can be used to define accessible regions for a spacecraft with a given energy (determined by its initial conditions). From equation 3.32, the relative velocity is greater than zero ($\dot{x}^2 + \dot{y}^2 + \dot{z}^2 > 0$). Thus, motion is only possible if $2U^* > C_j$. Fixing the relative velocity to zero, ($\dot{x}^2 + \dot{y}^2 + \dot{z}^2 = 0$), surfaces of zero relative velocity corresponding to different values of C_j can be constructed [26]. Use of the pseudo-potential becomes important when modeling the linearized system in later sections.

3.5 Libration Points

Five equilibrium points exist as particular solutions to the equations of motion 3.24, 3.25, and 3.26 governing the circular restricted three-body problem. These equilibrium points, known as libration points, occur where the gravitational and centrifugal accelerations cancel relative to the rotating system. Figure 3.2 (not drawn to scale) shows the general configuration of these libration points.

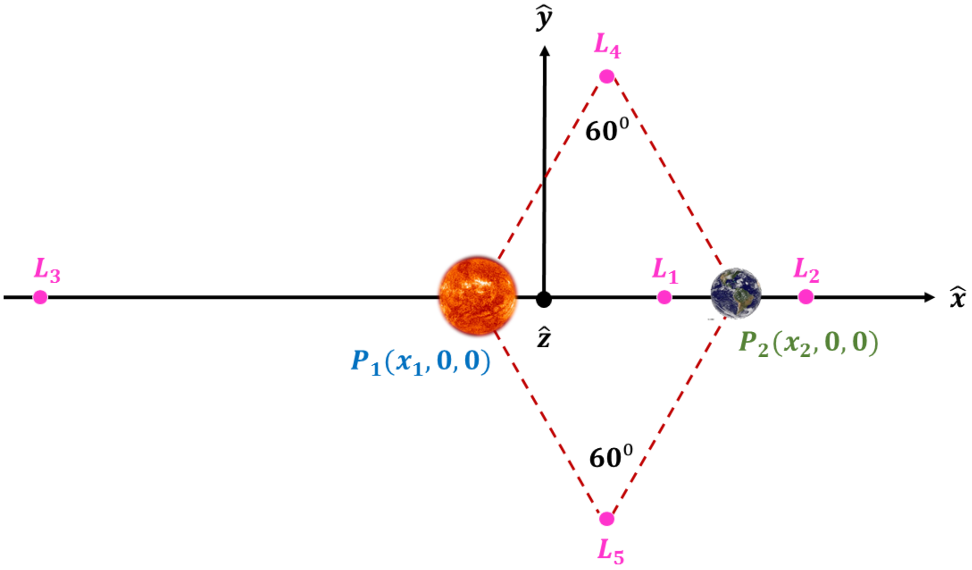

Figure 3.2: The five libration points in the three-body problem.

The libration points are located in the orbital plane of the two primaries. The L_1, L_2, and L_3 points are located along the rotating $\hat{x}$-axis and are referred to as collinear libration points, while the L_4 and L_5 points form an equilateral triangle with the primary bodies. This figure is not drawn to scale, as L_3 is significantly further away than indicated. As equilibrium points of the CR3BP, the libration points remain stationary with respect to the rotating frame.

To determine the location of the libration points, all derivatives in the equations of motion are set equal to zero and the remaining equations are solved for the states. The equations of motion reduce to

$$-x_{eq} = -\frac{(1-\mu)(x_{eq}-\mu)}{r_{1,eq}^3} - \frac{\mu(x_{eq}-(1-\mu))}{r_{2,eq}^3} \tag{3.33}$$

$$-y_{eq} = -\frac{(1-\mu)y_{eq}}{r_{1,eq}^3} - \frac{\mu y_{eq}}{r_{2,eq}^3} \tag{3.34}$$

$$0 = -\frac{(1-\mu)z_{eq}}{r_{1,eq}^3} - \frac{\mu z_{eq}}{r_{2,eq}^3} \tag{3.35}$$

where

$$r_{1,eq} = \sqrt{(x_{eq}+\mu)^2 + y_{eq}^2 + z_{eq}^2} \tag{3.36}$$

$$r_{2,eq} = \sqrt{(x_{eq}-(1-\mu))^2 + y_{eq}^2 + z_{eq}^2}. \tag{3.37}$$

These equations are solved for the equilibrium states. For the collinear points (L_1, L_2, L_3), an additional simplification can be made because of their location on the $\hat{x}$-axis, such that their y and z positions are zero. Solving the equations iteratively yields the three positions. Their positions along the $\hat{x}$-axis are described as follows,

$$L_1 : -\mu < x_{eq} < 1-\mu \tag{3.38}$$

$$L_2 : x_{eq} > 1-\mu \tag{3.39}$$

$$L_3 : x_{eq} < -\mu. \tag{3.40}$$

For the equilateral points (L_4 and L_5), their locations reside at the vertices of an equilateral triangle with the primary bodies. Thus, $r_{1,eq} = r_{2,eq}$ and the equations yield a solution of

$$L_{4,5} = \left(\frac{1}{2} - \mu, \pm\frac{\sqrt{3}}{2}\right). \tag{3.41}$$

Table 3.2 gives the locations of the libration points for the Sun-Earth system.

Table 3.2: Libration point locations for Sun-Earth system.

Libration Point	X [AU]	Y [AU]	Z [AU]
L_1	0.99002658776978	0.000000	0.000000
L_2	1.01003412259398	0.000000	0.000000
L_3	-1.00000125145255	0.000000	0.000000
L_4	0.499996996513878	0.866025403784439	0.000000
L_5	0.499996996513878	-0.866025403784439	0.000000

All three collinear libration points in the CR3BP are unstable. By linearizing the equations of motion about the libration point and finding the eigenvalues of the linearized dynamics matrix, their stability can be analyzed.

3.6 Stability Analysis

The linearized equations of motion about a collinear point can be represented by equations 3.28, 3.29, and 3.30. The development here follows that in Wie [27]. The in-plane characteristic equation is

$$\lambda^4 + (4 - U_{xx} - U_{yy})\lambda^2 + U_{xx}U_{yy} = 0, \tag{3.42}$$

giving in-plane eigenvalues of

$$\lambda_{1,2} = \pm\sqrt{-\beta_1 + \sqrt{\beta_1^2 + \beta_2^2}} \tag{3.43}$$

$$\lambda_{3,4} = \pm j\sqrt{\beta_1 + \sqrt{\beta_1^2 + \beta_2^2}} = \pm j\omega_{xy} \tag{3.44}$$

where ω_{xy} is the non-dimensional frequency of the in-plane oscillatory mode and

$$\beta_1 = 2 - (U_{xx} + U_{yy})/2 \tag{3.45}$$

$$\beta_2 = -U_{xx}U_{yy} > 0. \tag{3.46}$$

Szebehely [26] proved that U_{xx} is always positive, while U_{yy} is always negative. The in-plane motion has one stable, one unstable, and two oscillatory poles.

The out-of-plane characteristic equation is

$$\lambda^2 - U_{zz} = 0, \tag{3.47}$$

giving out-of-plane eigenvalues of

$$\lambda_{5,6} = \pm j\sqrt{|U_{zz}|} = \pm j\omega_z \tag{3.48}$$

where ω_z is the non-dimensional frequency of the out-of-plane oscillatory mode. The out-of-plane equation is a simple harmonic oscillator, and its out-of-plane motion is always periodic. By choosing initial conditions wisely, the stable and unstable poles of the system can be made to vanish. The quasi-periodic solution to the linearized equations of motion for a collinear libration point can be expressed by

$$x(t) = x(t_0)\cos\omega_{xy}t + \frac{1}{k}y(t_0)\sin\omega_{xy}t \tag{3.49}$$

$$y(t) = y(t_0)\cos\omega_{xy}t - kx(t_0)\sin\omega_{xy}t \tag{3.50}$$

$$z(t) = z(t_0)\cos\omega_z t + \frac{\dot{z}(t_0)}{\omega_z}\sin\omega_z t \tag{3.51}$$

where

$$k = \frac{\omega_{xy}^2 + U_{XX}}{2\omega_{xy}}. \tag{3.52}$$

Quasi-periodic Lissajous trajectories are the result of orbits with different in-plane and out-of-plane frequencies. In general, the Lissajous trajectory does not close. If the amplitude of the orbit is increased enough so that the in-plane and out-of-plane frequencies match, then a periodic halo orbit results. The Lissajous trajectory and halo orbit are the results of linear analysis of the restricted three-body problem. Spacecraft motion is still governed by the non-linear equations of motion, and thus the spacecraft will not follow the Lissajous trajectory or halo orbit naturally.

3.7 Periodic Orbits

An infinite number of periodic solutions exist in the CR3BP. One type of simply symmetric periodic orbit is termed a halo orbit. Halo orbits were first discovered during the late 1960s for use in the Apollo Program because of their ability to provide uninterrupted communication from the opposite side of the moon [24]. These trajectories are of particular interest here to serve as a baseline orbit for satellite arrays. Because the CR3BP cannot currently be solved explicitly, halo orbits are important in understanding the nature of solutions to the equations of motion. An example of a periodic halo orbit appears in Figure 3.3.

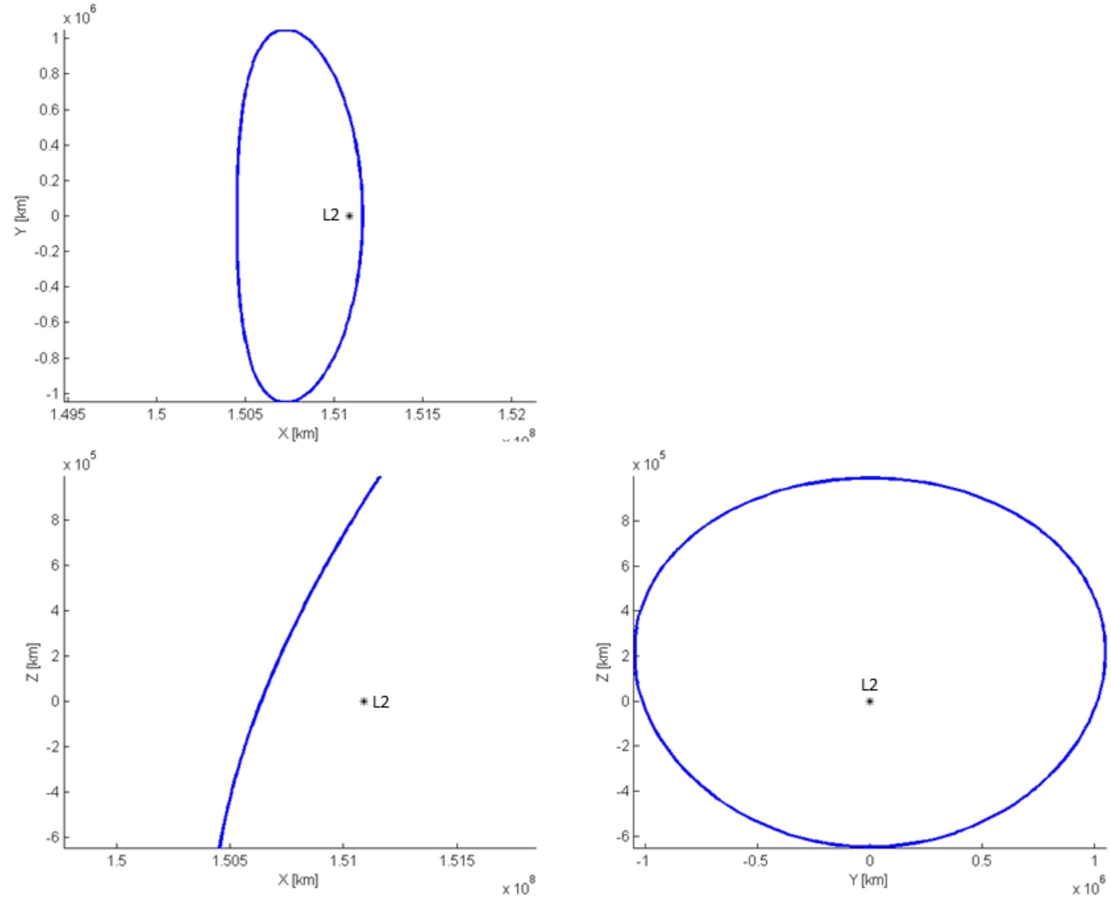

Figure 3.3: Example of a periodic halo orbit about the Sun-Earth L_2.

As shown in Figure 3.3, the halo orbit is symmetric about the xz-plane and looks circular when viewed from the location of the Sun. There is extensive literature on the existence and nature of periodic solutions of the CR3BP. Many different methods are available to establish periodic solutions; however, the current work uses a differential corrections process [28] in conjunction with a third-order approximation [29] as a first guess.

For a given trajectory,

$$\bar{X}(t) \equiv \begin{bmatrix} x(t) & y(t) & z(t) & \dot{x}(t) & \dot{y}(t) & \dot{z}(t) \end{bmatrix}^T \tag{3.53}$$

the goal of a targeting scheme is to determine a variation in the initial state that results in a desired change in the final state. Numerical implementation of a differential corrector relies on knowledge of the linearized equations of motion associated with the nonlinear system. Letting the state error be represented by

$$\delta\bar{X}(t) = \bar{X}(t) - \bar{X}_{ref}(t) \tag{3.54}$$

where $\bar{X}_{ref}(t)$ represents a periodic halo orbit, the variation can be approximated using a Taylor series expansion about the reference. The first-order approximation results in

$$\delta\dot{\bar{X}}(t) = A(t)\delta\bar{X}(t) \tag{3.55}$$

where $\delta\bar{X}(t) \equiv \begin{bmatrix}\delta x & \delta y & \delta z & \delta\dot{x} & \delta\dot{y} & \delta\dot{z}\end{bmatrix}^T$ represents variations with respect to a reference trajectory. In general, $A(t)$ is time-varying and is a function of the position and velocity at each point along the trajectory. The general solution to this system is

$$\delta\dot{\bar{X}}(t) = \Phi(t,t_0)\delta\bar{X}(t_0) \tag{3.56}$$

where $\Phi(t,t_0)$ is the state transition matrix (STM). In the CR3BP, the STM can be used to approximate variation in the initial and final states to first order,

$$\delta\bar{X}(t_f) = \frac{\delta\bar{X}(t_f)}{\delta\bar{X}(t_0)}|_{\bar{X}_{ref}(t)}\delta\bar{X}(t_0) + \dot{\bar{X}}(\bar{X}(t_f),t_f)\delta t \tag{3.57}$$

where

$$\frac{\delta\bar{X}(t_f)}{\delta\bar{X}(t_0)}|_{\bar{X}_{ref}(t)} = \Phi(t_f,t_0). \tag{3.58}$$

Thus the STM approximates the impact of initial variations on variations downstream, and serves as a type of linear mapping. The STM along a reference orbit can be numerically computed by integrating the following 42 ODEs simultaneously,

$$\dot{\bar{X}}(t) = f(\bar{X}(t)) \tag{3.59}$$

$$\dot{\Phi}(t, t_0) = A(t)\Phi(t, t_0) \tag{3.60}$$

with initial conditions

$$\bar{X}(t_0) = \bar{X}_0 \tag{3.61}$$

$$\Phi(t_0, t_0) = I_{6\times 6}. \tag{3.62}$$

Here, $f(\bar{X}(t))$ represents the CR3BP nonlinear equations of motion, written in first-order form. The Jacobian matrix is given by

$$A(t) = \begin{bmatrix} 0 & 0 & 0 & 1 & 0 & 0 \\ 0 & 0 & 0 & 0 & 1 & 0 \\ 0 & 0 & 0 & 0 & 0 & 1 \\ U^*_{xx} & U^*_{xy} & U^*_{yz} & 0 & 2 & 0 \\ U^*_{yx} & U^*_{yy} & U^*_{yx} & -2 & 0 & 0 \\ U^*_{zx} & U^*_{zy} & U^*_{zz} & 0 & 0 & 0 \end{bmatrix} \tag{3.63}$$

where U^* is defined in equation 3.27. The partials $U^*_{kl} = \frac{\partial}{\partial k}(\frac{\partial U^*(t)}{\partial l})$ are also functions of time. This dependence, however, has been dropped for convenience of writing. This matrix is evaluated along the reference trajectory.

To begin the process of differential corrections, both an initial state and final state must be defined. The symmetry of halo orbits aids in simplifying this step. Recall that halo orbits are symmetric about the xz-plane ($y = 0$) and intersect this plane perpendicularly ($\dot{x} = \dot{z} = 0$). Thus the initial state vector must be of the form

$$\bar{X}_0 = \begin{bmatrix} x_0 & 0 & z_0 & 0 & \dot{y}_0 & 0 \end{bmatrix}^T \tag{3.64}$$

and the first guess for its components are calculated from third-order approximations. The equations of motion are propagated forward in time until the trajectory crosses the xz-plane a second time. Because this second crossing must be perpendicular, the desired final state vector must be of the form

$$\bar{X}_f = \begin{bmatrix} x_f & 0 & z_f & 0 & \dot{y}_f & 0 \end{bmatrix}^T . \tag{3.65}$$

In general, the first iteration does not produce perpendicular crossings and it is likely that ($\dot{x}_f$) and ($\dot{z}_f$) are not zero. Thus it is necessary to manipulate the three non-zero initial conditions (x_0, z_0, and $\dot{y}_0$) to drive the final velocities ($\dot{x}_f$ and $\dot{z}_f$) to zero. It should be noted that this second crossing of the xz-plane corresponds to a time equal to half of the orbital period of the halo orbit.

The differential corrections process uses the STM to change initial conditions such that a desired final state is reached

$$\delta\bar{X}_f = \Phi(t_f, t_0)\delta\bar{X}_0 \tag{3.66}$$

where the change in the initial state is determined using the difference between the actual and desired final states. In this way, three initial states (δx_0,δz_0, and $\delta\dot{y}_0$) are used to target two final states ($\delta\dot{x}_f$ and $\delta\dot{z}_f$). For implementation it is more convenient to constrain one of the initial state variables so that a 2×2 matrix (instead of a 2×3 matrix) is inverted to find two of the initial variations. The revised initial conditions are used to begin the next iteration, and the process continues until $\dot{x}_f = \dot{z}_f = 0$ within an acceptable tolerance. Convergence is expected within 5 iterations. Because the orbit is symmetric about the xz-plane, it is not necessary to calculate the second half of the orbit. More on the differential corrections method used can be found in [28].

The reference halo orbit used in simulation for this study is shown in Figure 3.4. The corrected initial conditions for this halo orbit are given in Table 3.3.

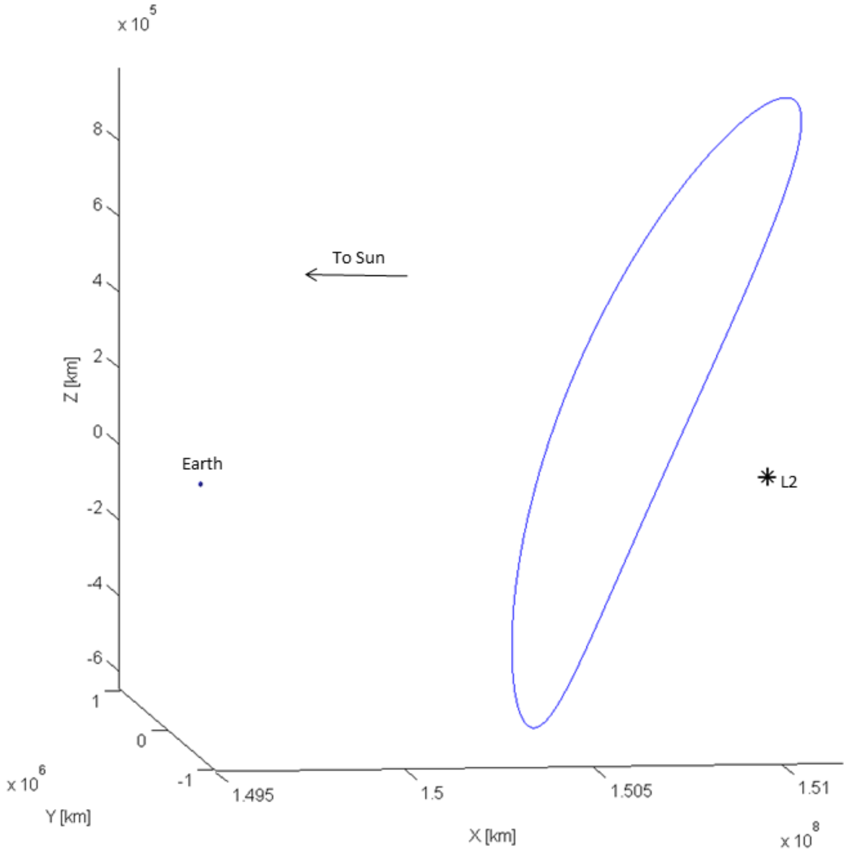

Figure 3.4: Reference halo orbit used in simulation.

Table 3.3: Corrected initial conditions for the reference halo orbit.

Parameter	Value
x_0	151160583.19402 km
y_0	-0.08117 km
z_0	992310.14300 km
$\dot{x}_0$	-0.00000 km/s
$\dot{y}_0$	-0.38545 km/s
$\dot{z}_0$	-0.00000 km/s
$^1/_2$ Period	88.54811 days

4. CONTROL METHODS

Both periodic and quasi-periodic trajectories about the libration points are inherently unstable. Thus it is necessary to develop station keeping algorithms which help the satellites to remain close to the reference orbit. It is especially important that the desired imaging formation remain intact so that adequate coverage of the shadow pattern enables silhouette reconstruction.

Many station-keeping algorithms have been developed for spacecraft moving in multi-body regimes. These include simple differential targeting schemes, as well as more complicated methods which take into account estimated errors down range [30]. Several studies have been done on formation control with respect to image quality [31, 32, 33]; however, most of these results are concerned with Guassian distributions of apertures as opposed to rigid formations, as is the case in the current study. As a first look into rigid body formation control near collinear libration points, the current study implements simpler techniques such as Proportional Derivative Control and Linear Quadratic Regulation to illustrate that the control required to maintain such geometric formations with negligible error in position is possible.

4.1 Control Problem Formulation

Let motion of the spacecraft in the CR3BP be modeled as

$$\ddot{x} = f_x(x, y, z, \dot{x}, \dot{y}, \dot{z}) + u_x \tag{4.1}$$

$$\ddot{y} = f_y(x, y, z, \dot{x}, \dot{y}, \dot{z}) + u_y \tag{4.2}$$

$$\ddot{z} = f_z(x, y, z, \dot{x}, \dot{y}, \dot{z}) + u_z \tag{4.3}$$

where f_x, f_y, and f_z are the nonlinear equations of motion for the CR3BP and $u(t) = \begin{bmatrix} u_x & u_y & u_z \end{bmatrix}^T$ is an applied control vector. Let a reference orbit which satisfies the above equations be denoted by $X_{ref}(t)$. Here, the halo orbit computed in Section 3.7 is used to define a unique reference orbit for each spacecraft individually. Spacecraft control is computed based on the state error of the spacecraft from its unique reference orbit. Thus, spacecraft control is considered uncoupled. The following sections detail the two types of control implemented–Proportional Derivative and Linear Quadratic Regulation.

4.2 Proportional Derivative Control

A Proportional Integral Derivative (PID) controller minimizes state error by adjusting three separate, constant gains. The error is evaluated as the difference between the current state and a reference state. The proportional gain acts on the present error, the integral gain acts on the accumulation of past errors, and the derivative gain acts on the current rate of change in error. Because the PID controller only relies on the measured errors and not on knowledge of the underlying dynamics, it is a broadly applicable controller [34].

The three gains in the PID controller can be tuned to provide control for specific state requirements. In general, the response of the controller is described in terms of its responsiveness to error, the amount by which it overshoots its desired state, and its tendency to oscillate. It should be noted that use of a PID controller does not guarantee optimal control, nor system stability.

Let a reference orbit which satisfies the nonlinear equations of motion 4.1, 4.2, and 4.3 be denoted by $X_{ref}(t)$. The error is then defined such that

$$\delta X(t) = X(t) - X_{ref}(t) \tag{4.4}$$

where the state error here is only concerned with differences in the positions. The derivative term is then defined as the velocity error,

$$\delta\dot{X}(t) = \dot{X}(t) - \dot{X}_{ref}(t). \tag{4.5}$$

The proportional, integral, and derivative terms are summed to compute the necessary PD control ouput. Defining $u(t)$ as the controller output, the final form of the PID algorithm is

$$u(t) = K_p\delta X(t) + K_I\int \delta X(t)dt + K_d\delta\dot{X}(t) \tag{4.6}$$

where K_p is the proportional gain, K_i is the integral gain, and K_d is the derivative gain. An integral term is not used in this implementation of the PID controller, but is included in the above equation for completeness.

The proportional term yields a control output proportional to the current error. A high proportional gain results in a large output response to a given error; however, if this gain is too high, the system will become unstable. Proportional gains which are too small, on the other hand, produce controllers which are less sensitive to large input errors. The proportional term should contribute the bulk of control action.

The integral term produces an output proportional to both the magnitude and duration of error. Its purpose is to accelerate the system towards its desired state and to eliminate residual steady-state error that occurs from purely proportional control. However, the integral term can also produce overshoot because it is a function of past errors.

The derivative term produces an output proportional to the current rate of change in error and can be thought of as a predictor of future error. Inclusion of the derivative gain improves settling time and stability of the system. Because it is a function of the error rate of change, it has great control authority over the state that immediately follows.

To implement the PD controller, the reference trajectory is integrated forward in time and stored at discrete times for later reference. At each time step, the spacecraft's trajectory is integrated forward and its error in position and velocity computed. A control is computed by applying a proportional K_p and derivative K_d gain to the respective errors. The resulting control is fed into the nonlinear equations of motion for the next integration step, and the process repeats for each interval of the trajectory. Tuning of the gains is necessary for minimizing the state error of a given system.

4.3 Linear Quadratic Regulator

Optimal control is concerned with managing a dynamic system at minimum cost. The Linear Quadratic problem in particular is concerned with a system whose dynamics can be described by a set of linear differential equations and whose cost is represented as a quadratic function. The cost is defined as a sum of errors from a desired state, such as a spacecraft's motion away from some reference trajectory. Often the control magnitude is included so that the energy expended by the control effort is also minimized. Derivation of the LQR controller follows that of Lewis [35].

Let a reference orbit which satisfies the nonlinear equations of motion 4.1, 4.2, and 4.3 be denoted by $X_{ref}(t)$. Linearization about the reference orbit yields a system,

$$\delta \dot{X}(t) = A(t)\delta X(t) + B(t)\delta u(t) \tag{4.7}$$

where δX represents the state error, δu represents the control error with respect to the reference, $A(t)$ is given by the Jacobian matrix, and

$$B(t) = B = \begin{bmatrix} 0_{3\times 3} & I_{3\times 3} \end{bmatrix} \tag{4.8}$$

such that the control adjusts only velocity of the spacecraft and not the position. A quadratic cost function is used to minimize a combination of both the state error and required control [36],

$$J = \frac{1}{2}\delta X(t_f)^T S(t_f)\delta X(t_f) + \frac{1}{2}\int_{t_0}^{t_f} (\delta X(t)^T Q\delta X(t) + \delta u(t)^T R\delta u(t))dt \tag{4.9}$$

subject to the equations of motion above and the initial condition $\delta X(t_0) = \delta X_0$. The Q and R matrices are weighting factors and must be positive definite. Because the individual state errors are decoupled from the required control, the Q and R matrices are diagonal. In this paper, Q and R are taken to be identity matrices of proper dimension, multiplied by constant gains. Because the cost function can be scaled by any constant gain without affecting the results, only the relative magnitudes of R and Q are important.

Applying the Euler-Lagrange theorem to the system yields the first order conditions for optimality,

$$\delta\dot{X}(t) = A(t)\delta X(t) + B\delta u(t) \tag{4.10}$$

$$-\dot{\lambda}(t) = Q\delta X(t) + A(t)^T\lambda(t) \tag{4.11}$$

$$0 = R\delta u(t) + B^T\lambda(t) \tag{4.12}$$

with boundary conditions

$$\delta X(t_0) = \delta X_0 \tag{4.13}$$

$$\lambda(t_f) = S(t_f)\delta X(t_f). \tag{4.14}$$

From the stationary condition given in equation 4.12, the optimal control is

$$\delta u(t) = -R^{-1}B^T\lambda(t). \tag{4.15}$$

Consider a state feedback controller defined by

$$\lambda(t) = S(t)\delta X(t). \tag{4.16}$$

Substituting 4.16 into equations 4.11 with boundary condition 4.14 yields the Riccati matrix differential equation,

$$\dot{S}(t) = -A(t)^T S(t) - S(t)A(t) + S(t)BR^{-1}B^T S(t) - Q \tag{4.17}$$

subject to $S(t_f) = 0_{6\times 6}$. Equations 4.1, 4.2, 4.3, and 4.17 represent a two-point boundary value problem with the given first order, ordinary differential equations. The optimal control becomes

$$\delta u(t) = K(t)\delta X(t) \tag{4.18}$$

where $S(t)$ is a solution of the matrix differential Riccati equation and $K(t)$ represents the control gain

$$K(t) = -R^{-1}B^T S(t). \tag{4.19}$$

The process of implementing the linear controller in the nonlinear model is broken into a few steps. First, the reference trajectory is integrated forward in time so that the $A(t)$ matrix can be evaluated at each step. Both are stored at discrete times for later reference. Next, the matrix differential Riccati equation is solved backward in time, along with the control gain, and is stored for later use. Finally, spacecraft motion is numerically integrated forward using the perturbed nonlinear equations of motion. Control accelerations are applied at each time step, according to the stored control gains. The integration step size is determined from the initial integration of the reference trajectory, since reference states are only known at these designated times.

4.4 Control Implementation

The halo orbit is stored as a list of states at discrete times. For implementation of control, a new reference trajectory is defined for each aperture such that it has a constant offset from the halo orbit. In this way, each aperture tracks an orbit such that the overall array geometry remains intact. For both the PD and LQR controllers, spacecraft control is computed based on the state error of the spacecraft from its unique reference orbit. Thus in the current implementation, spacecraft control is uncoupled from neighboring spacecraft, including the chief. The chief for each array geometry is placed at the refernce halo orbit that was solved for in Section 3.7. A continous control force is assumed, with actuation provided by x, y, and z-oriented thrusters. Each spacecraft is assumed to have a mass of 100 kg.

4.4.1 Controller Responses

To ensure that each control algorithm is properly mitigating state error, a single test spacecraft is given an initial offset (with error in all three coordinates) and the resulting response documented. The reference orbit for the test spacecraft is placed 100 meters in the y-direction and 100 meters in the z-direction from the halo orbit. The response for the PD controller is shown in Figures 4.1 and 4.2.

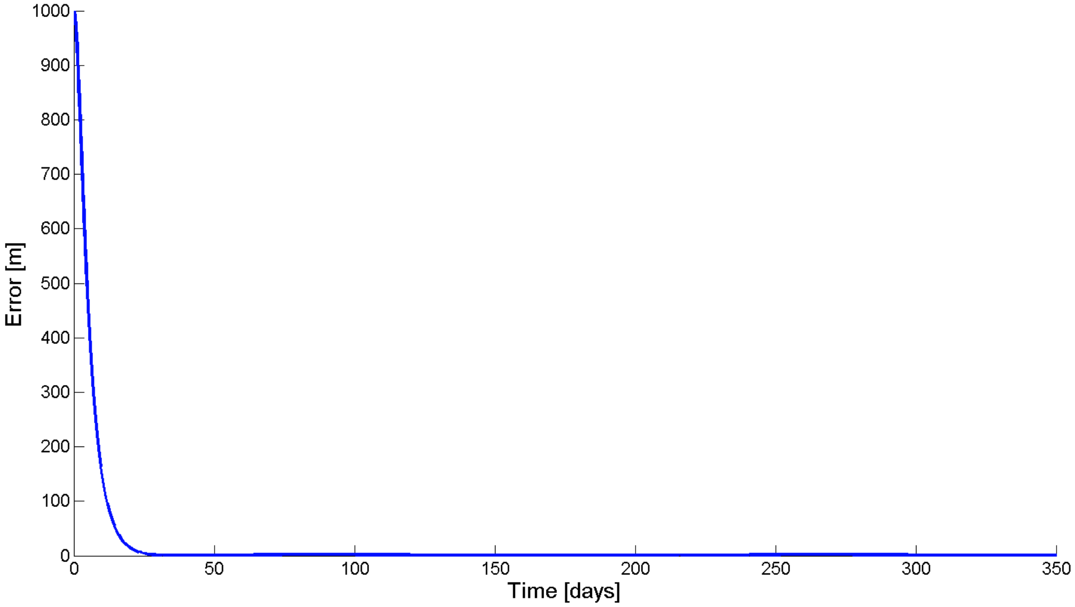

Figure 4.1: Magnitude of state error over time with implementation of a PD controller.

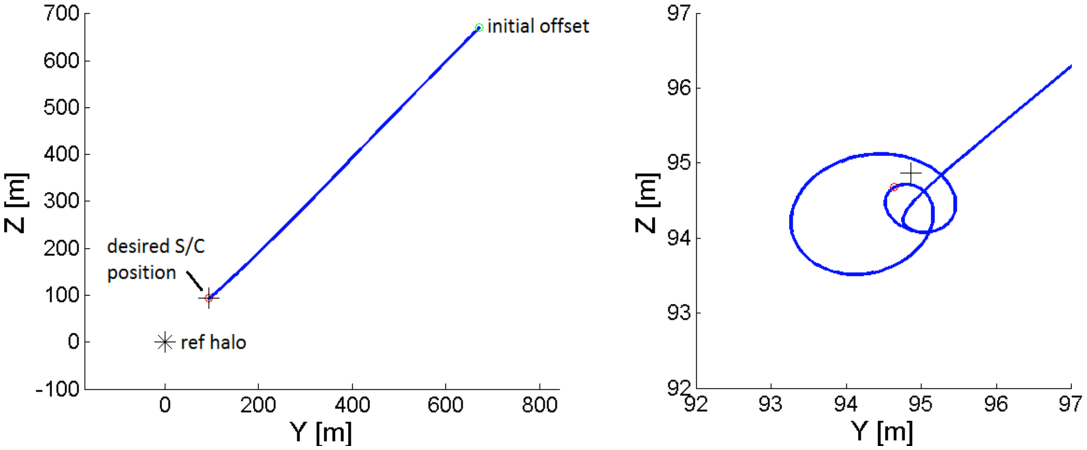

Figure 4.2: Spacecraft motion in the yz-plane over time with implementation of a PD controller.

Figure 4.1 plots the magnitude of state error over time using a PD controller. Given the initial offset, the PD controller quickly minimizes the error to nearly zero.

Figure 4.2 shows a projection of the spacecraft's motion on the yz-plane, relative to the reference halo orbit denoted by a black star at the origin. The spacecraft's desired location is denoted by a black plus '+'. The starting and ending states are denoted by a green and red 'o' marker, respectively. As shown, the PD controller quickly returns the spacecraft to its desired trajectory. The PD controller then maintains the spacecraft's position near its reference orbit over the two period time of simulation. The maximum error during this trajectory maintenance period is approximately 2 meters.

The response for the LQR controller is shown in Figures 4.3 and 4.4. The same initial offset is given to the test spacecraft under LQR control.

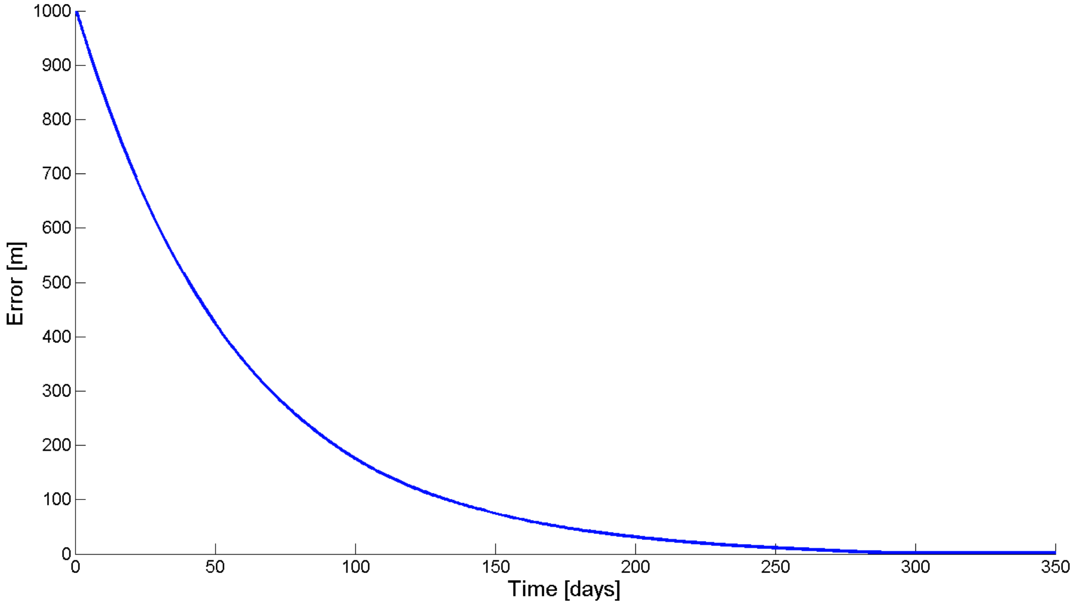

Figure 4.3: Magnitude of state error over time with implementation of a LQR controller.

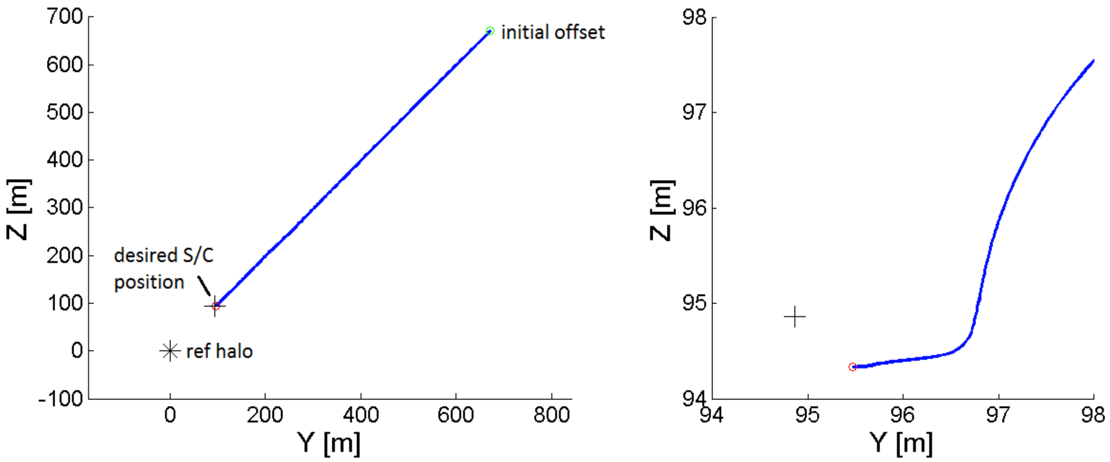

Figure 4.4: Spacecraft motion in the yz-plane over time with implementation of a LQR controller.

Figure 4.3 shows the magnitude of the spacecraft's state error over time using an LQR controller. Given the initial offset, the LQR controller minimizes the error to nearly zero. The response is significantly slower than that for the PD controller because of the additional cost to minimize control effort. Figure 4.4 shows a projection of the spacecraft's motion on the yz-plane, relative to the reference halo orbit. This halo orbit is denoted by a black star at the origin. The spacecraft's desired trajectory is denoted with a black plus '+'. The starting state is shown as an open green marker, while the final state is shown as an open red marker. Again, the LQR controller returns the spacecraft to the vicinity of its desired state. The LQR controller then attempts to maintain the desired trajectory for the remainder of the simulation. The maximum error during this trajectory maintenance time is approximately 1 meter; however it takes the entirety of the simulation to reach this position. The PD controller seems to have a quicker response while maintaining a similar error to the LQR controller. This would imply that the PD controller is the better choice, especially when the savings in computational complexity is considered.

4.5 Control of Array Geometries

From the last section, it was shown that both the PD and LQR controllers are able to mitigate state error of the test spacecraft. It is now desired to implement both controls for the desired formation of apertures.

Consider an array made up of approximately 20 apertures located at a halo orbit about the Sun-Earth L_2 libration point. The purpose of the following control simulation is to determine if the formation can be maintained using a PD and LQR controller such that the array is able to be used in the stellar occultation system described previously. For success, the control must maintain the width of the array, as well as the relative spacing between apertures. This is to provide sufficient coverage of the shadow pattern as outlined in Section 2.2.

A reference orbit unique to each spacecraft in the formation is computed, and the control remains uncoupled. Both a PD and LQR controller are implemented and compared. The formation is equally-spaced about the center reference halo orbit and lies in the yz-plane, which is normal to the direction of the Sun. Orientation of the formation with respect to its pointing direction and field of view are not considered here. Future work should include examination of the most desirable regions of sky for occultation observations.

Control is implemented for three candidate array geometries–the string of pearls, circular, and Y-shaped arrays. The chief is located at the center reference halo orbit and the 20 apertures are distributed about it equally. The chief requires negligible control effort. For calculation of the required control forces, each spacecraft is assumed to have a mass of 100 kg.

4.5.1 String of Pearls Control

A string of pearls array containing 21 apertures (1 chief + 20 others) is distributed equally about the reference halo orbit along the $\hat{y}$-axis in the yz-plane. Typically a string of pearls refers to a series of spacecraft in the same orbit following one another. Here, the string of pearls array is treated more like a rigid line formation where each spacecraft follows separate orbits. This was done so that relevant comparisons could be made with the circular and Y-shaped arrays, which are constrained to the yz-plane. Figures 4.5 and 4.6 show the relative motion, or error, of the apertures with respect to the chief at the center reference halo orbit. Motion is plotted over two orbital periods. The desired location of each aperture is marked with a black plus '+'. The spacecraft are numbered from the inside outward and their motions are denoted with varying colored line based on distance from the chief. The array spans a width ≈ 1200 meters with each aperture separated by ≈ 60 meters from its closest neighbor.

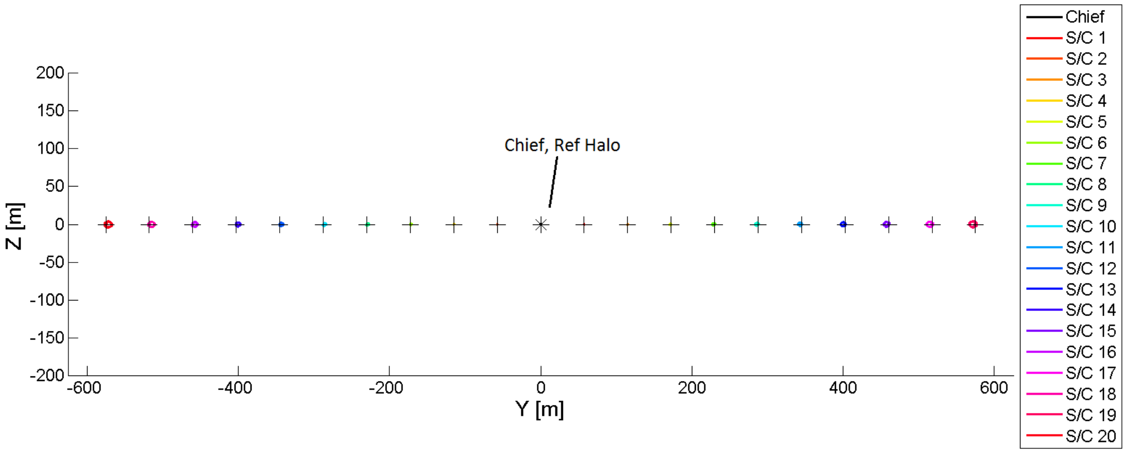

Figure 4.5: Formation motion of string of pearls array relative to the reference halo orbit using PD control.

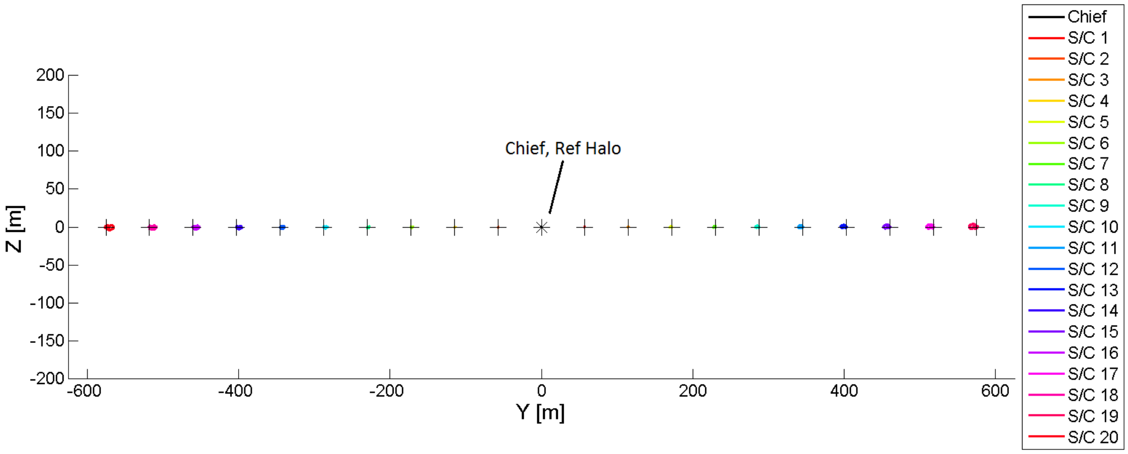

Figure 4.6: Formation motion of string of pearls array relative to the reference halo orbit using LQR control.

Figure 4.5 shows formation motion under PD control, while Figure 4.6 shows motion under LQR control. In both cases, the overall array geometry is maintained over multiple periods. The errors here are negligible with respect to the separation distances between apertures.

The magnitude of position error for each of the 21 apertures is shown in Figure 4.7. For the string of pearls formation using PD control, the maximum error is 9.2 meters, while that using LQR control is 17.5 meters. This maximum error is experienced by the apertures farthest from the center halo orbit (spacecraft 19 and 20). In fact, error appears to increase with increasing distance from the center reference halo orbit.

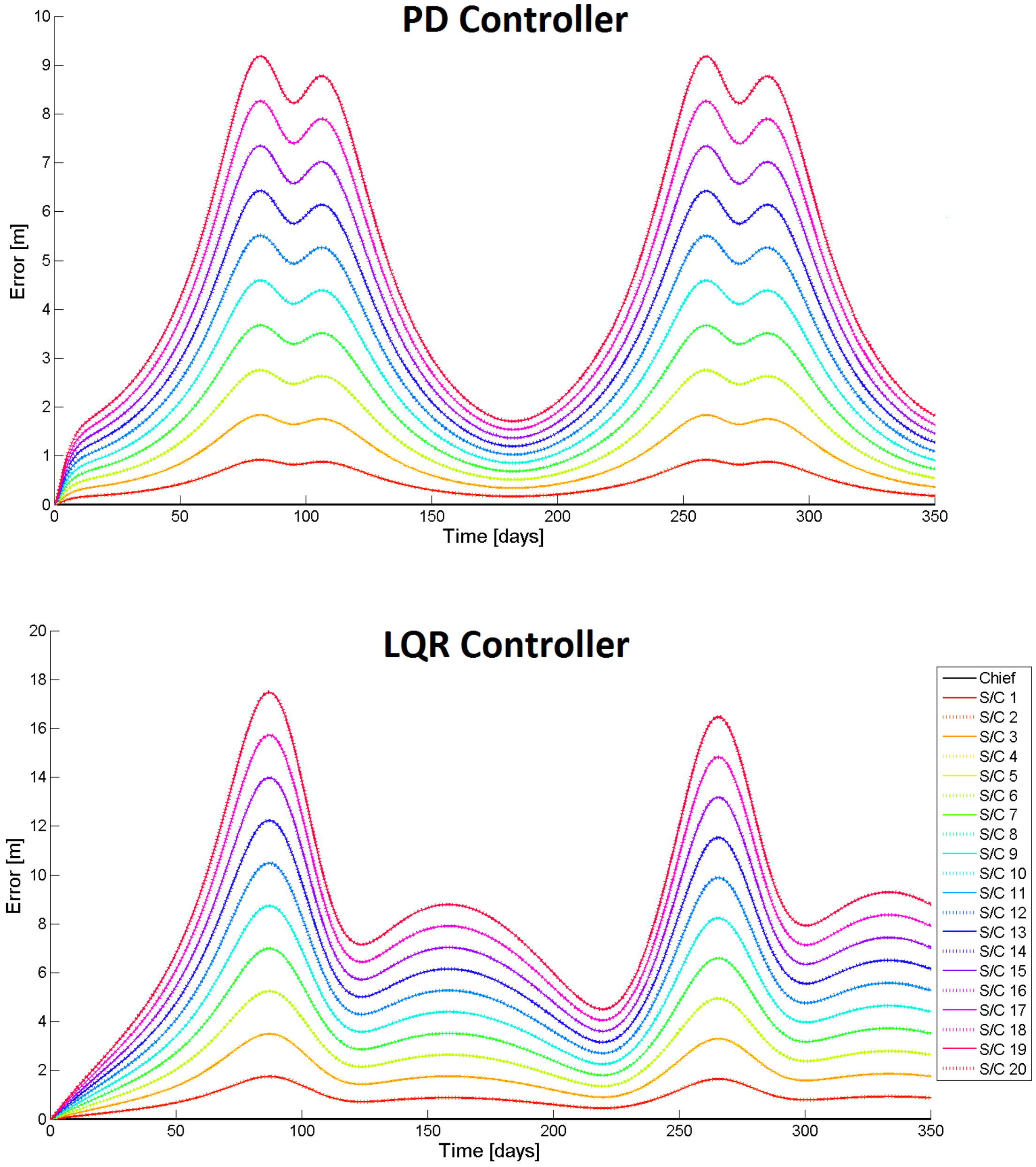

Figure 4.7: Position error for each of the 21 apertures in the string of pearls formation using PD control (top) and LQR control (bottom).

While 9 meters is the greatest error magnitude, formation control using this stellar occultation method is primarily concerned with keeping the array geometry intact (minimizing relative error) rather than simply minimizing each spacecraft error individually. Thus, the difference between the smallest and largest error of the spacecraft at any one time is a more relevant metric. The natural drift experienced by all the spacecraft, as illustrated by the two hump features, tends to help in maintaining the formation because all spacecraft experience these features periodically and near the same location in each orbit. These features are a product of fighting the nonlinear dynamics of the problem and are evident in both the PD and LQR controlled cases. As expected, the trajectory of the chief spacecraft, initially located on the halo orbit, is maintained without error over the simulation period.

Figure 4.8 shows the control forces necessary to keep each spacecraft near its desired orbit using a PD and LQR controller. From PD control theory, it is expected that control output will closely follow that of the error, and this is illustrated in Figures 4.7 and 4.8. This is due to the fact that the bulk of the controller output is computed based on the state error. The maximum control force needed to maintain a spacecraft in this formation using PD control is 2.03×10^{-11} N. Using LQR control, the required force is 1.96×10^{-11} N. These maximum control forces are required by the spacecraft farthest from the center reference halo orbit. As shown, both controllers require similar amounts of control force to maintain the formation.

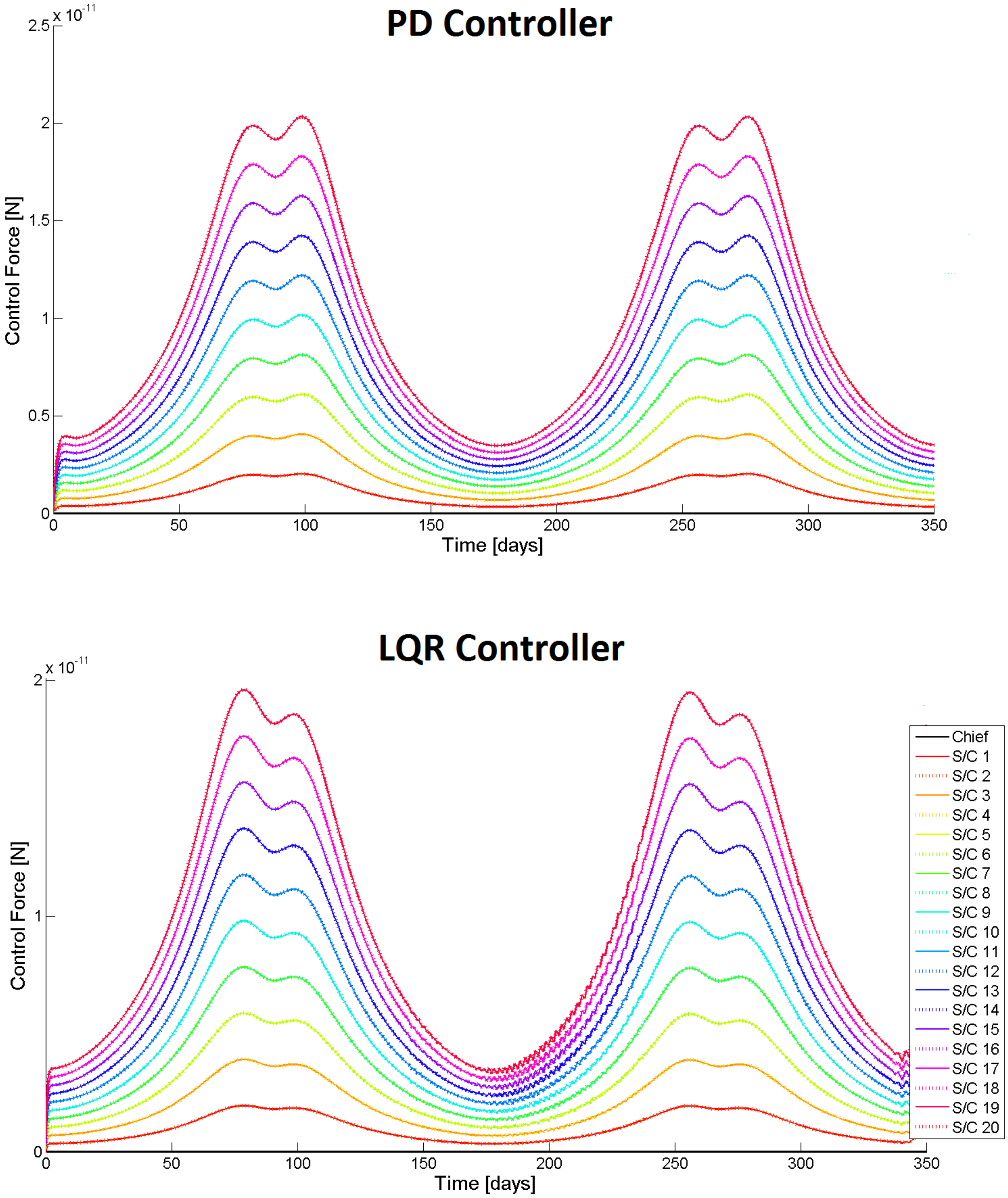

Figure 4.8: Control time history for each of the 21 apertures in the string of pearls formation using PD control (top) and LQR control (bottom).

4.5.2 Circular Array Control

A circular array containing 21 apertures (1 chief + 20 others) is distributed equally along the perimeter of a circle of radius ≈ 600 meters. The circle is centered about the reference halo orbit in the yz-plane. Figures 4.9 and 4.10 show the relative motion of the apertures with respect to the chief at the center reference halo orbit over two orbital periods. The desired location of each aperture is marked with a black plus '+'. From simulation it was determined that diametrically-opposed pairs of spacecraft experience similar dynamics, and so the spacecraft were numbered such that their motion is colored according to this pairing. See Figures 4.9 and 4.10 below. The array spans ≈ 1200 meters in width with each aperture separated by ≈ 180 meters from its closest neighbor.

Figure 4.9 shows formation motion under PD control for the circular array, while Figure 4.10 shows its motion under LQR control. As illustrated below, both PD and LQR controllers maintain the circular formation over multiple periods with negligible errors in position relative to the separation distances.

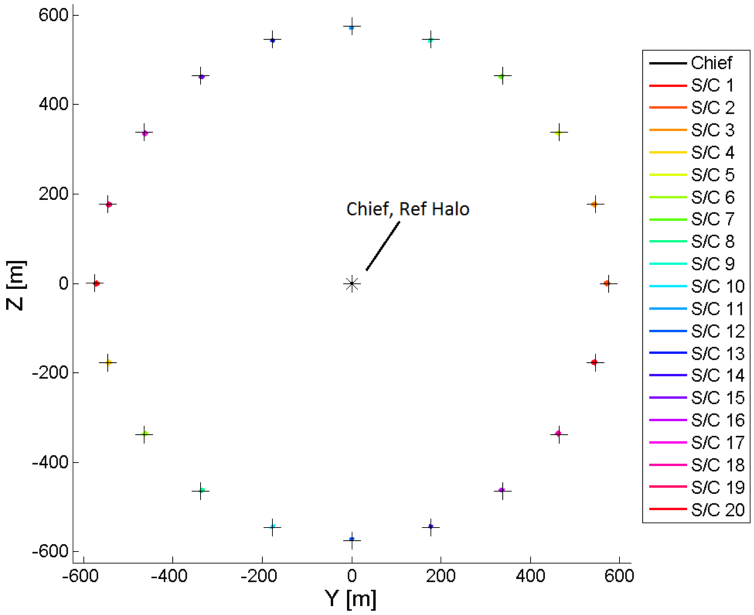

Figure 4.9: Formation motion of circular array relative to the reference halo orbit using PD control.

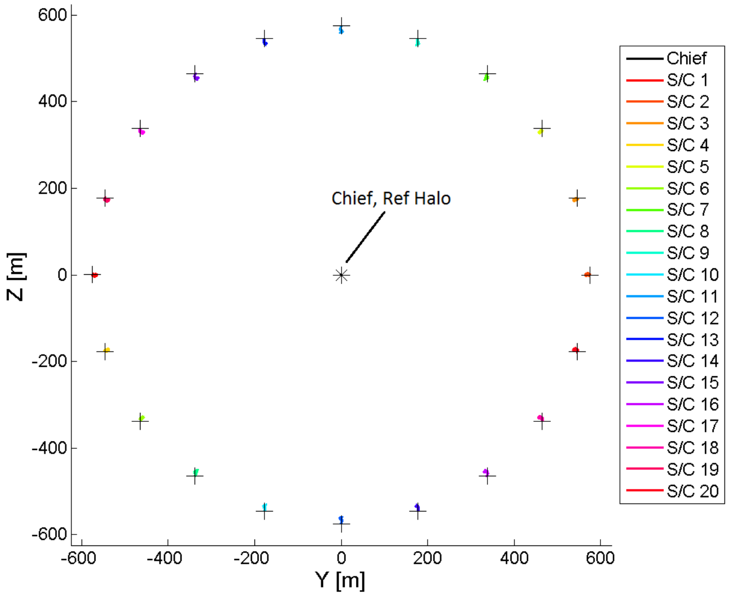

Figure 4.10: Formation motion of circular array relative to the reference halo orbit using LQR control.

Figure 4.11 gives the magnitude of error over time for each of the 21 spacecraft. For the circular formation using PD control, the maximum error is 12.7 meters, while that using LQR control is 23.6 meters. This maximum error is experienced by the apertures with the greatest z-component from the reference halo orbit (spacecraft 11 and 12). The circular array has less relative error between apertures than the string of pearls array. This is due to the fact that all 20 spacecraft (excluding the chief) are displaced equal distances from the reference halo, as opposed to varying distances along the $\hat{y}$-axis. Thus the circular array has the lowest relative error between apertures of the array geometries.

The necessary control forces to maintain this formation are given in Figure 4.12 for both the PD and LQR controllers. Again it is evident that PD control output is proportional to the current error. The maximum control force needed to maintain a spacecraft in this formation using PD control is 2.76×10^{-11} N and for LQR control is 2.07×10^{-11} N. Both controllers require similar amounts of control force to maintain this formation, but the PD controller has the lowest errors in position.

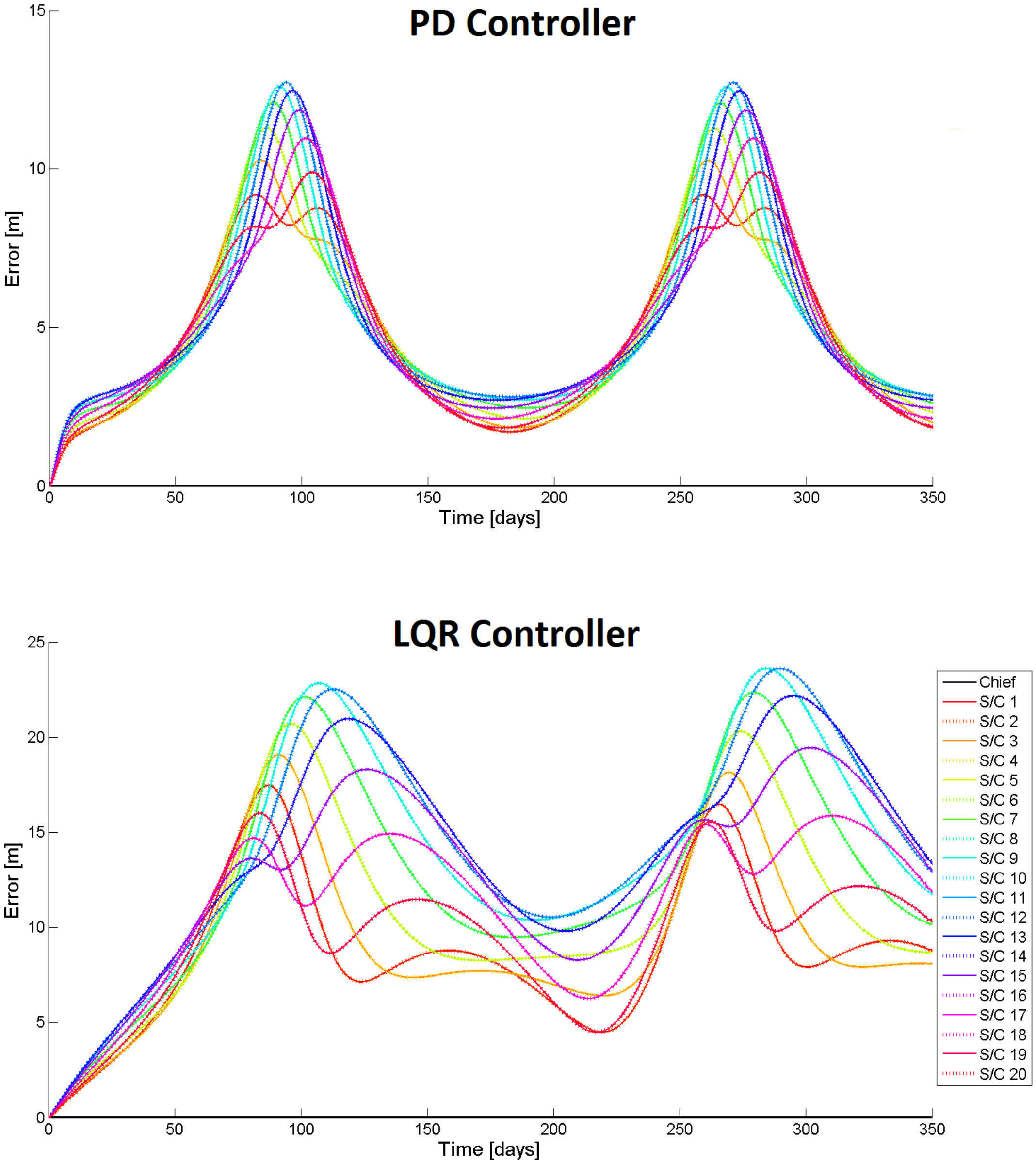

Figure 4.11: Position error for each of the 21 apertures in the circular formation using PD control (top) and LQR control (bottom).

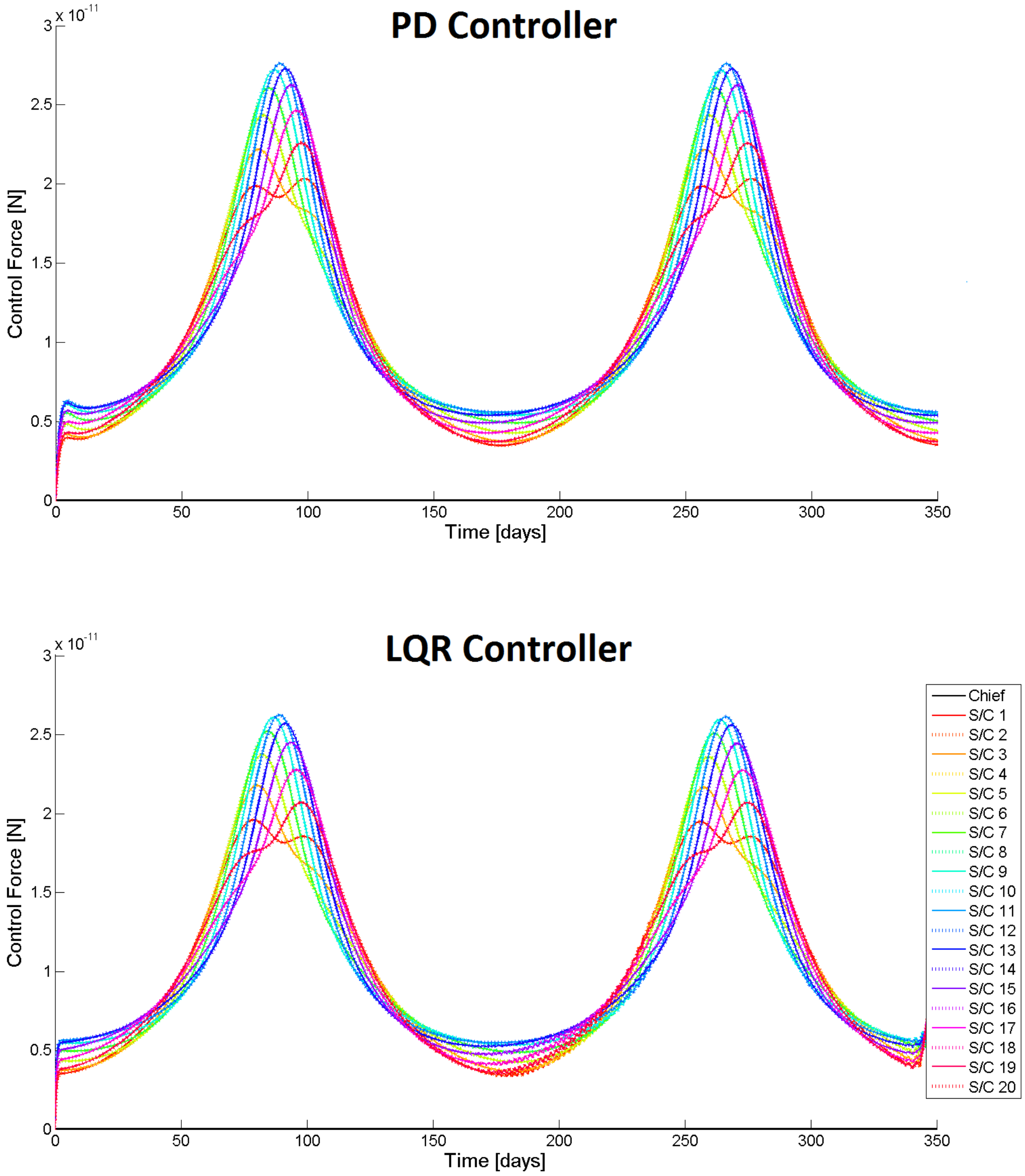

Figure 4.12: Control time history for each of the 21 apertures in the circular formation using PD control (top) and LQR control (bottom).

4.5.3 Y-shaped Array Control

A Y-shaped array containing 21 apertures (1 chief + 20 others) is distributed equally along three arms with center at the reference halo orbit. To keep the same control infrastructure, one of the three arms has only 6 apertures instead of 7. The formation lies in the yz-plane. Figures 4.13 and 4.14 show the relative motion of the apertures with respect to the chief at the center reference halo orbit over two orbital periods. The desired location of each aperture is marked with a black plus '+'. The spacecraft are numbered such that their motions are denoted with varying colored lines based on distance from the reference halo orbit. Each arm spans ≈ 600 meters with each aperture separated by ≈ 100 meters from its neighbor.

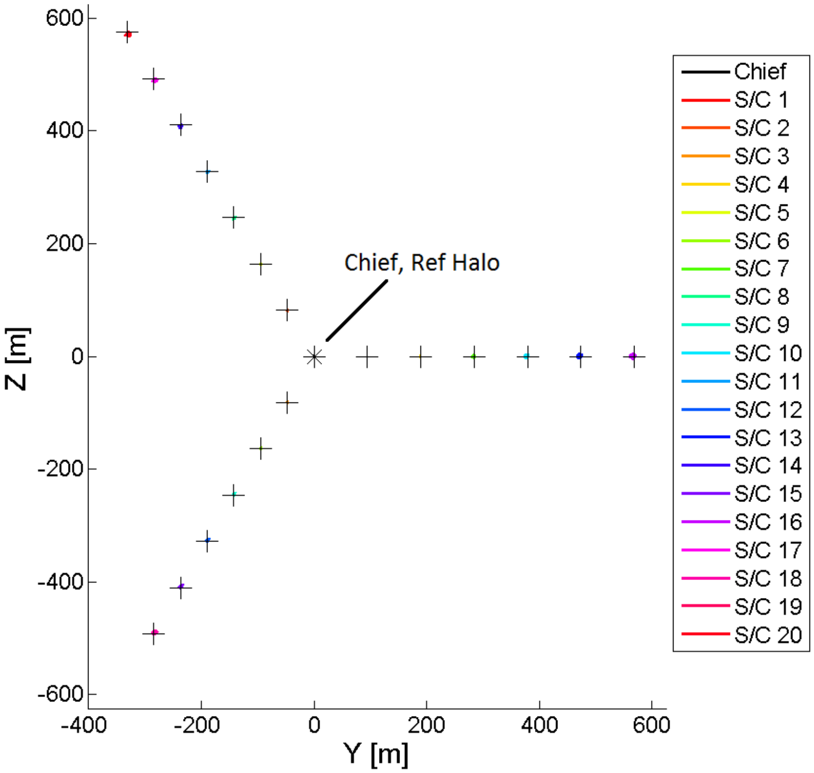

Figure 4.13: Formation motion of Y-shaped array relative to the reference halo orbit using PD control.

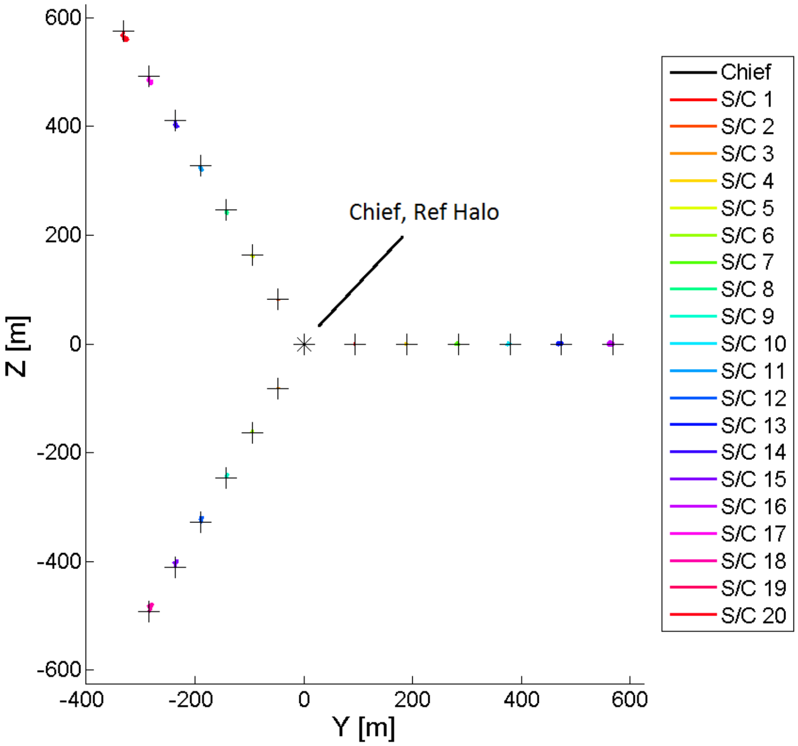

Figure 4.14: Formation motion of the Y-shaped array relative to the reference halo orbit using LQR control.

Figure 4.13 shows formation motion under PD control, while Figure 4.14 shows motion under LQR control. Again, in both cases the formation is maintained with negligible error over multiple periods when compared to aperture separation distances.

The error magnitude for each spacecraft is shown in Figure 4.15. For the Y-shaped array using PD control, the maximum error is 14.0 meters, while that using LQR control is 23.6 meters. This greatest error is experienced by the aperture with the greatest z-component from the reference halo orbit (spacecraft 20). If another spacecraft were added to the third arm to complete the Y-symmetry, this spacecraft 21 would also experience the maximum error. Overall, the spacecraft error appears to increase with increasing distance from the center halo orbit.

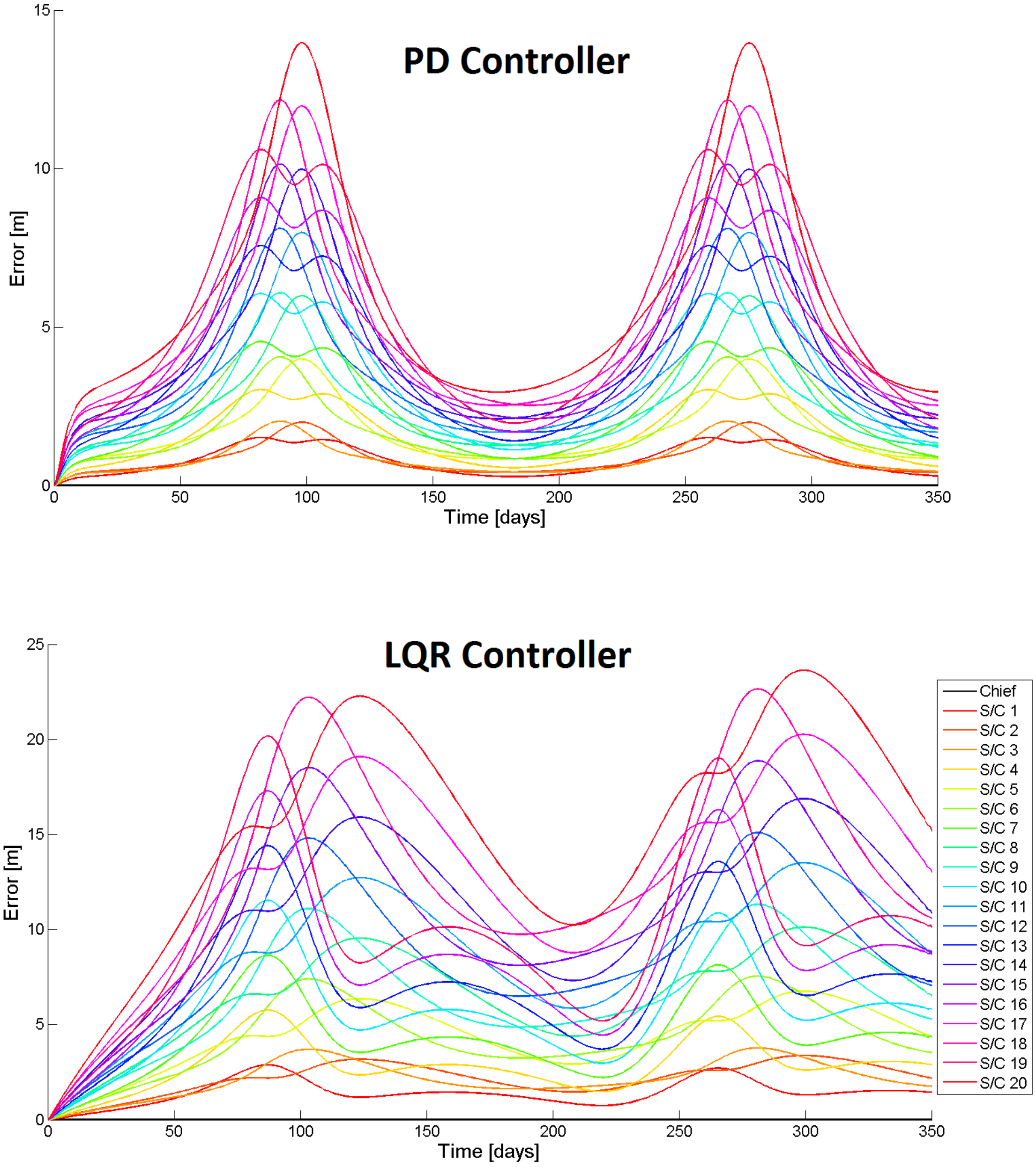

Figure 4.15: Position error for each of the 21 apertures in the Y-shaped formation using PD control (top) and LQR control (bottom).

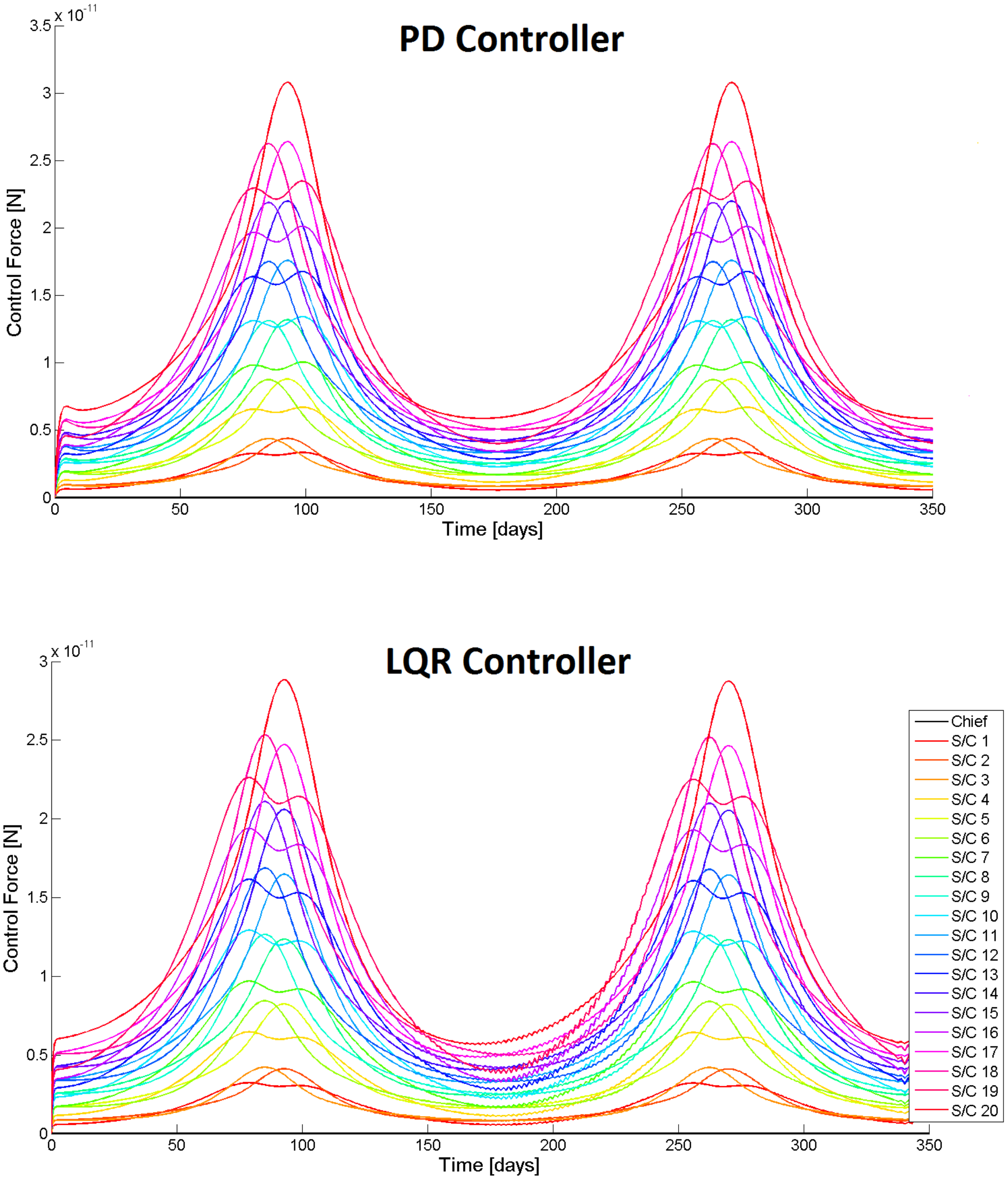

Figure 4.16: Control time history for each of the 21 apertures in the Y-shaped formation using PD control (top) and LQR control (bottom).

The control force magnitude needed to implement such motion using both PD and LQR controllers is shown in Figure 4.16 above. The maximum control force needed for the PD controller is 3.08×10^{-11} N, and for the LQR controller is 2.88×10^{-11} N. While the control effort required for the LQR controller is less than that required for the PD controller, the latter yields significantly less state error for a very small difference in control effort and with minimal computational complexity.

4.6 Control Summary

From these results, it is evident that both a PD and LQR controller produce similar responses and have the ability to maintain spacecraft at desired locations of a formation. In addition, formation maintenance is achieved with negligible error and very small control forces. In fact, for a 100 kg spacecraft with x, y, and z-oriented microthrusters of $I_{sp} = 300$ sec, the required fuel for the spacecraft which requires the most control force of all spacecraft in any of the formations is 3.30×10^{-7} kg of fuel per year of operation. For 20 spacecraft, this would require less than 6.60×10^{-6} kg of fuel per year, assuming the most expensive control. In reality, these control forces would not be implemented continuously, nor are there many microthrusters which can produce such low thrust on the order of 10^{-11} N. Thus, in a real system, the error would be allowed to grow until some specified error tolerance and minimum control force are required.

Both state error and control appear to be proportional with distance from the center halo orbit. While the LQR control tends to require less control forces, the reduced error and its computational simplicity make the PD controller a strong choice. The position errors for all array geometries were considered negligible with respect to the aperture separation distances. However, the circular array provided the best relative errors among spacecraft. This is due to the fact that the apertures of the circular array are equal distance from the center halo orbit. If a conventional string of pearls formation is placed along the reference halo orbit, one spacecraft in front of the other (each following the same orbit), state errors and the resulting control forces would be even less. This is evident in the negligible control required for the chief spacecraft in all the plots.

Because station keeping errors are negligible with respect to the separation distances between apertures, analysis of array geometries based on their ability to reconstruct an asteroid silhouette can proceed in the following chapter.

5. SYSTEM SIMULATION AND EVALUATION OF ARRAY GEOMETRIES

Three different array geometries are analyzed and compared for the occultation system described in Chapter 2. A string of pearls is used as the base-line configuration, while the circular and Y-shaped arrays are used as alternative designs. For a given number of apertures, each array geometry is examined to find its optimal configuration. Each configuration then undergoes simulation to reconstruct an asteroid's silhouette given the light intensity measurements recorded by each of its apertures. Because the optimal configuration is unlikely to occur for every occultation, a wost-case, non-optimal configuration is also examined to place bounds on each geometry's expected performance.

5.1 Imaging Simulation

In the last chapter it was shown that the three candidate array geometries can be maintained with negligible error and control effort. Thus evaluation of each geometry's capability optically can proceed. Given an array made up of 21 apertures, the purpose of the following system simulation is to determine how well the formations are able to reconstruct the silhouette of an asteroid from the pattern of light intensities measured at each of its aperture locations. For success, a perfect or near perfect silhouette must be estimated in no more than 10 iterations of a simple raster scanning algorithm. It should be noted that the maximum of 10 iterations is somewhat arbitrary. The process is computed offline of the space-based system and using more iterations has no real tangible "cost" to system performance. Given sufficient data coverage of the shadow pattern, the process tends to converge in less than 10 iterations, so this was chosen as a convenient means for which to monitor the process breaking down due to insufficient coverage. Refer to the examples posed in Chapter 2.

In general, optimal configurations make use of all the apertures in the formation. In other words, no two apertures measure the same line of data across the shadow pattern. So termed, redundant data, does increase the SNR of the light intensity measurements, but does not contribute useful data to the silhouette reconstruction process.

To demonstrate the silhouette reconstruction process, consider the asteroid Itokowa as viewed from 1 astronomical unit away. The true silhouette was generated using data from the Hayabusa mission [18] and is shown in Figure 5.1.

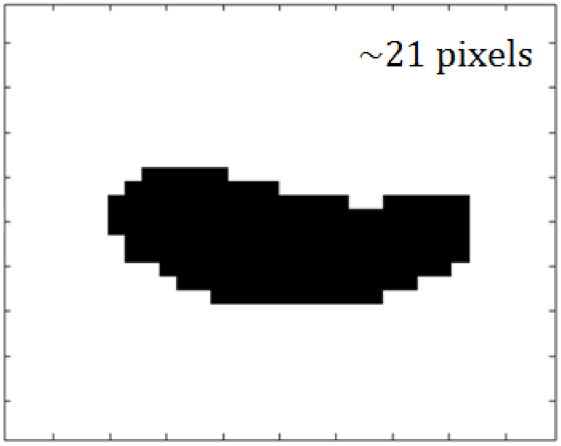

Figure 5.1: Desired silhouette of asteroid Itokawa.

Itokawa is 268 m in radius and the silhouette is approximately 21 pixels long. For the center band wavelength, it is common in optical interferometry to use green light, so a value of 5.5×10^{-7} meters is considered here. Referring to equation 2.1, the Fresnel number for this case is 0.87, and the simulated asteroid does indeed reside in the Fraunhofer region. While an SNR of 1 is required for the system, the light intensity SNR is assumed to be 10 for simulation purposes. It is assumed that SNR is not a limiting factor here. Development of the SNR requirements can be found in [21]. The intensity distribution at the array location is shown in Figure 5.2.

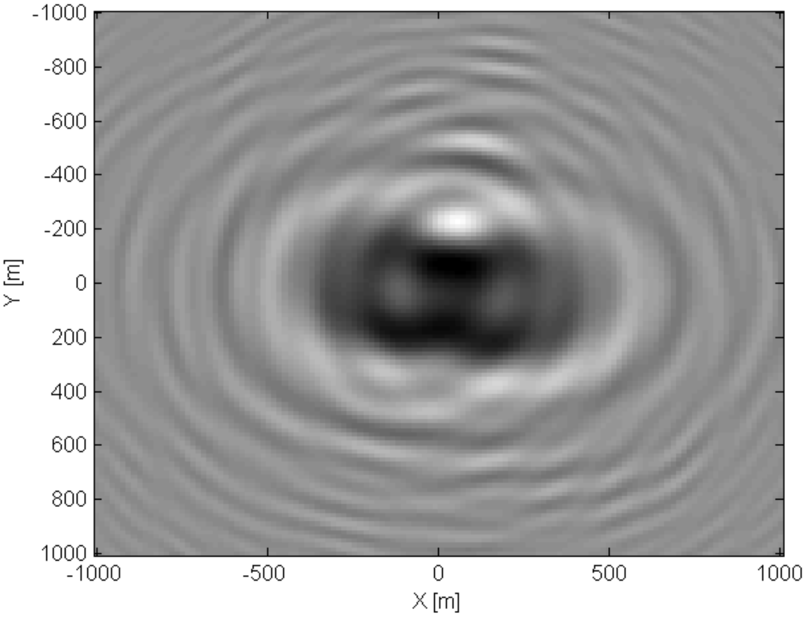

Figure 5.2: Shadow pattern of asteroid Itokawa at the observation plane for a Fresnel number of 0.87.

In practice, the continuous intensity map is not known at every location, as discussed in Section 2.2. Three array geometries are simulated here such that their ability to resolve silhouettes is assessed based on adequate coverage of the observation plane. Table 5.1 summarizes the significant parameters used in this simulation.

Table 5.1: Parameters used in silhouette reconstruction algorithms.

Parameter	Value
a	268 m
z	1 AU
λ	5.5×10^{-7} m
F	0.87
W	≈ 1200 m
Number of Apertures	21
Shadow Resolution	128×128 pixels
Silhouette Resolution	32×32 pixels
Max Iterations	10

Three candidate array geometries are evaluated–the string of pearls, circular, and Y-shaped arrays. Each array lies in the yz-plane, which is normal to the direction of the Sun. Orientation of the array concerning its pointing and field of view is not considered here. It is of course assumed that the array is not looking directly at the Sun; however the array should also not be pointed directly away from the Sun either. For the stellar occultation method used here, if the occulting object reflects enough sunlight, then the drop in brightness measured when it occults a distant star will not be sufficient to consider it a relevant occultation event.

A simple raster scan method is used to estimate the silhouette, as described in Section 2.1.2. No a priori knowledge is assumed. While optimization of this algorithm would provide faster convergence, no such development was executed in this study. Such manipulations include using lower resolution estimates as initial guesses to higher resolution cases, and manually changing obviously extraneous pixels after each iteration. Here, a simple maximum number of iterations is set and the resulting silhouette is taken as the end estimate. The final estimate is taken even if convergence is not met prior to reaching the iteration limit. One iteration is defined as a raster scan of every pixel in the silhouette grid. Thus it is possible to have convergence occur after only a fraction of a complete iteration. For instance, if the algorithm converged after scanning the silhouette grid 5 times plus one quarter of the sixth time, the simulation will have converged in 5.25 iterations.

5.2 String of Pearls

For the first array geometry, a string of pearls is examined. An array containing 21 equally-space apertures is distributed in a line along the width of the array. The formation is located near the Sun-Earth L_2 reference halo orbit discussed in Section 3.7. The array lies in the yz-plane.

5.2.1 Optimal String of Pearls Configuration

For the String of Pearls, optimal performance makes use of all apertures in the formation. This occurs when the formation is aligned perpendicular to the cross-track direction. This configuration is shown in Figure 5.3, where 21 equally-spaced apertures lie along the $\hat{y}$-axis of the rotating reference frame, distributed equally on either side of the reference halo orbit.

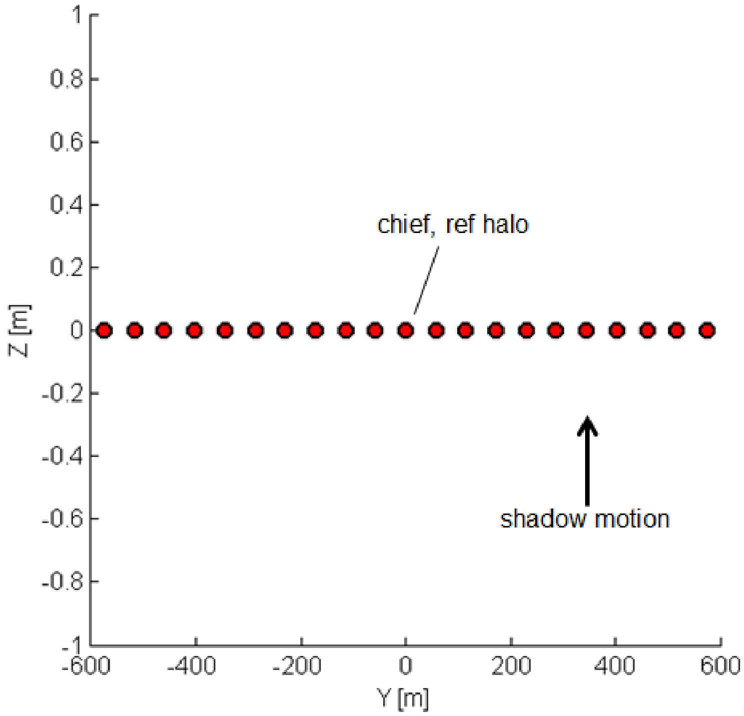

Figure 5.3: Optimal string of pearls array with 21 evenly-spaced apertures.

The red dots represent the actual positions of each aperture, while the black circles indicate their projection onto the $\hat{y}$-axis. Shadow motion moves upward along the $\hat{z}$-axis. The apertures are separated 60 meters apart, with 128 measurements along each line. It is desired to resolve a silhouette which is 21 pixels across; thus approximately 21 apertures are needed. As the shadow in Figure 5.2 sweeps across the array, each aperture collects a line of data as shown in Figure 5.4.

Using the process described in detail in Chapter 2, the recovered silhouette is shown in Figure 5.5. Perfect silhouette recovery was achieved after 3 iterations. These independently-reached results match with those found by Trahan [23]. For the string of pearls, this configuration is considered optimal.

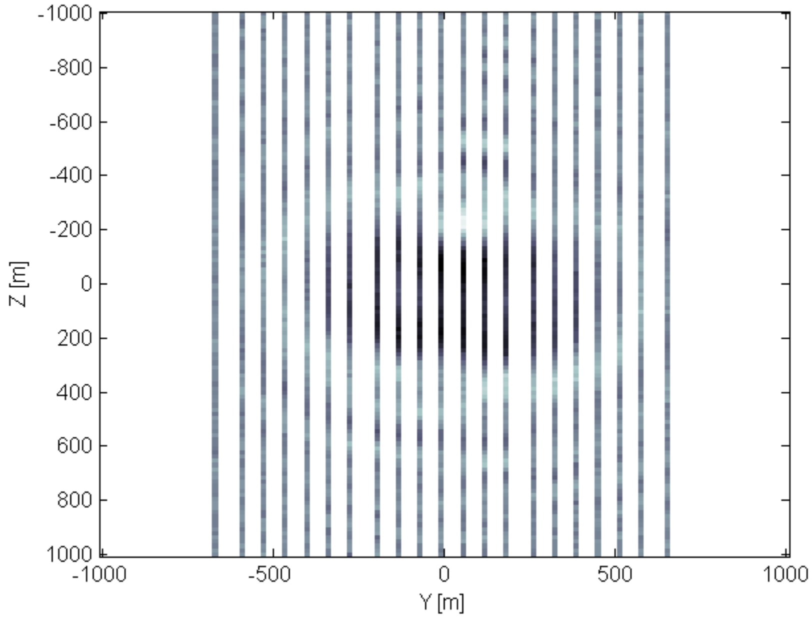

Figure 5.4: Sensor data swept out by optimal string of pearls array.

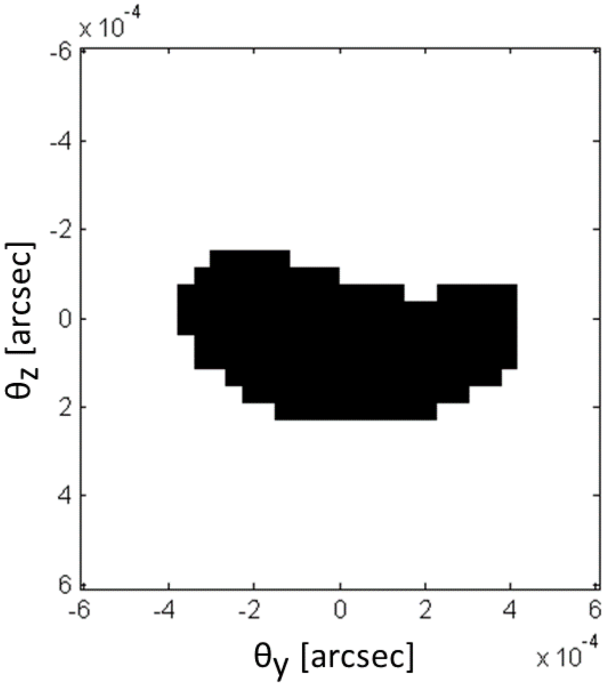

Figure 5.5: Reconstructed silhouette from an optimal string of pearls array.

5.2.2 Non-Optimal String of Pearls Configuration

While it is always desired to have the optimal configuration, it is unlikely that all occultation events will occur this way. For example, a shadow pattern that moves across the array at a 30 degree angle is shown in Figures 5.6 and 5.7.

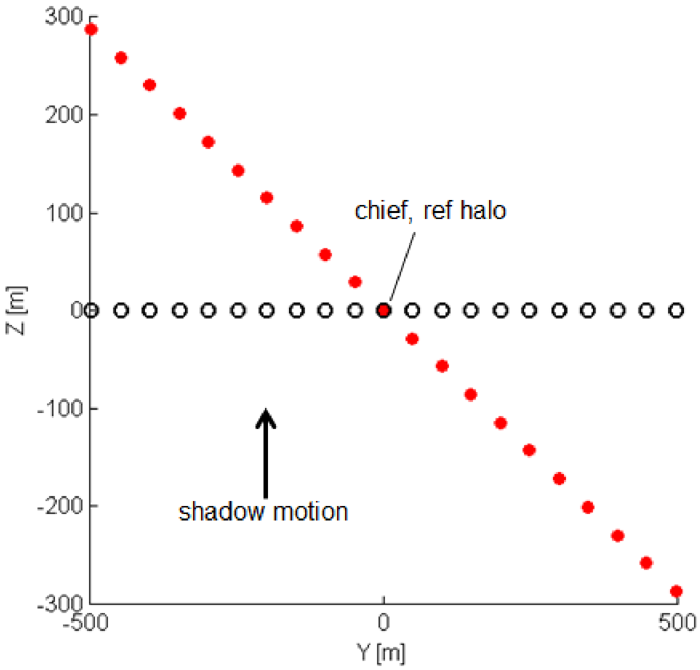

Figure 5.6: Non-optimal string of pearls array with 21 evenly-spaced apertures. Shadow motion is at 30 degrees relative to the formation.

As a result of the shadow's angled motion vector with respect to the formation, the array is distributed on a much smaller width of the observation plane. Only those apertures whose projections onto the $\hat{y}$-axis provide useful, non-redundant measurements contribute to the silhouette estimation process. The resulting silhouette estimate after 10 iterations is shown in Figure 5.8.

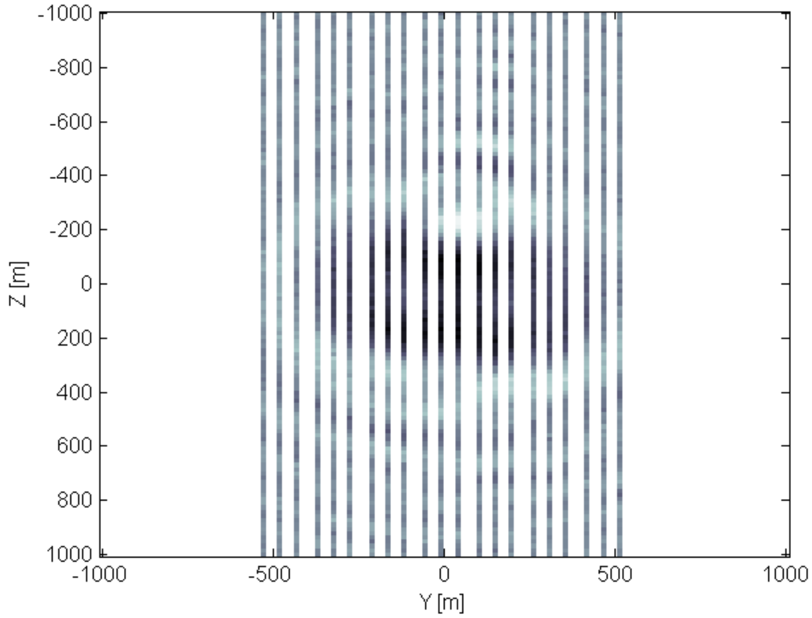

Figure 5.7: Sensor data swept out by non-optimal string of pearls array.

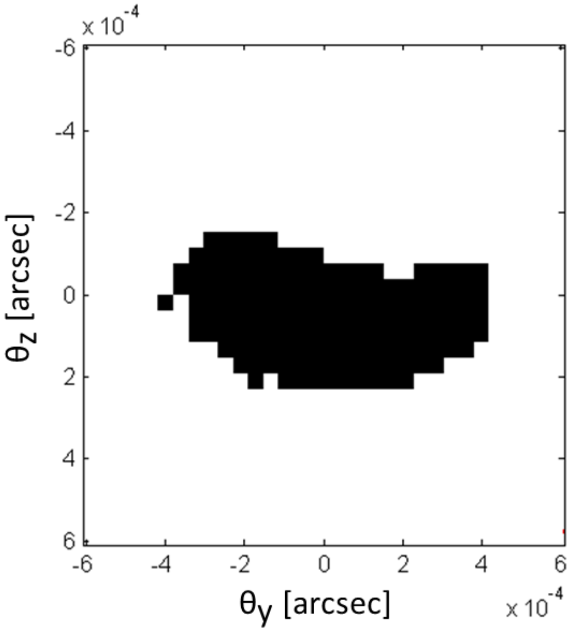

Figure 5.8: Reconstructed silhouette from a non-optimal string of pearls array.

As seen in the figure above, the general shape of Itokawa is apparent but there are a few misplaced pixels around its perimeter and the process did not converge within the allotted number of iterations. This showcases just how important the width of the array is to successful silhouette reconstruction. While a 30 degree angle is probably not the limiting geometry, it does give rise to the main drawback in using this array geometry–it only allows for asteroids moving in nearly one direction, across the longest width of the array. The true worst case configuration of this geometry occurs when the shadow simply moves down the line of apertures and all measurements become redundant. This only provides one measurement along the 20 pixel desired silhouette and reconstruction is not possible using the method here.

For this reason, the circular and Y-shaped arrays provide additional measurement facets that allow for multiple directions of shadow movement. For a relevant comparison, the circular and Y-shaped geometries are examined using the same number of apertures.

5.3 Circular Array

The next array geometry under examination is the circular array. Again, the apertures are placed in orbit near the Sun-Earth L_2 reference halo orbit. Each of the 21 apertures is equally spaced along the perimeter of a circle of radius ≈ 600 meters, with one chief located at the center reference halo orbit. The array lies in the yz-plane.

5.3.1 Optimal Circular Configuration

For the circular array, optimal performance makes use of all apertures in the formation. In order for this to occur, the shadow must move over the aperture with a small relative angle in the cross-track direction, such that no two sensors are redundant in measuring the light intensity. The circular array of 21 apertures is shown in Figure 5.9. The apertures around the perimeter of the circle are separated by 18 degrees.

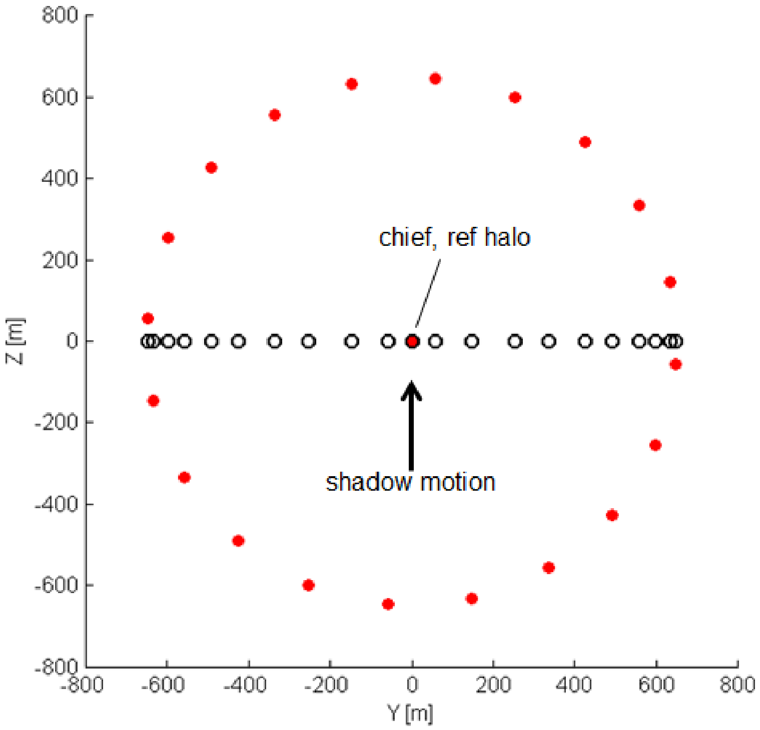

Figure 5.9: Optimal circular array with 21 evenly-spaced apertures.

Again, the actual aperture positions are shown in red, while the black circles represent their projections onto the $\hat{y}$-axis. The shadow is assumed to move upward along the $\hat{z}$-axis. As a result, the sensors sweep out data of intensity measurments as shown in Figure 5.10.

It is important to note that while it appears all apertures are recording non-redundant measurements, if the silhouette resolution is not fine enough, then multiple aperture measurements will be used to resolve the same pixels. For instance in Figure 5.9, it appears that the apertures on the right and left extremes of the y-projection are overlapping. Thus these may not be actually adding useful information to the processing algorithms if the silhouette is taken to be of much lower resolution. For circular arrays of less (but still a sufficient number of) apertures, this overlapping of data measurements near the edges is not as prevalent because their y-projected locations are more spread out.

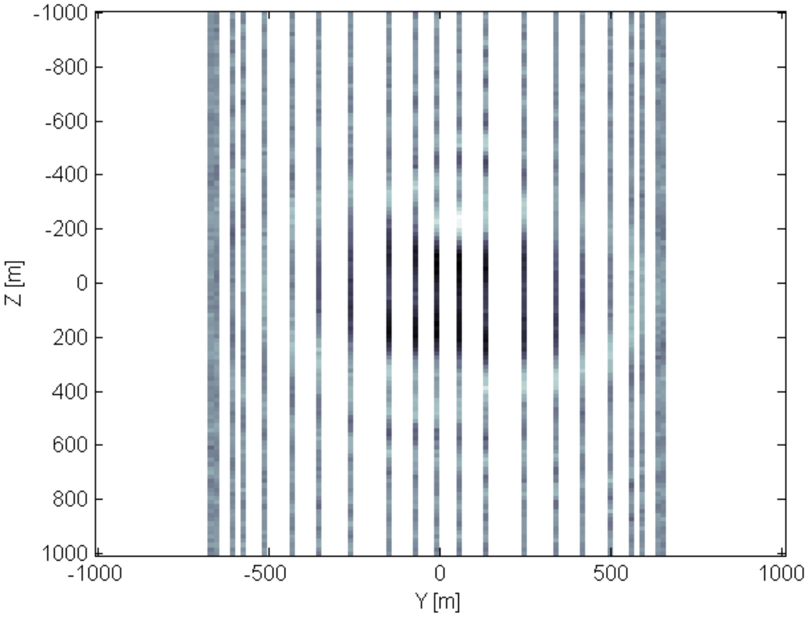

Figure 5.10: Sensor data swept out by optimal circular array.

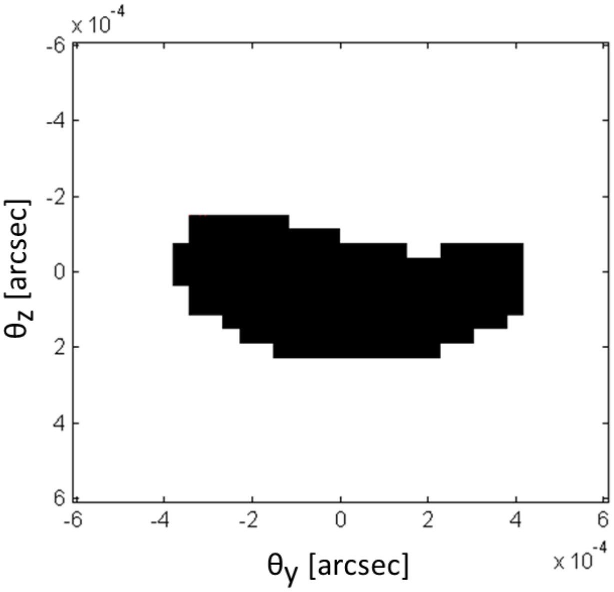

Figure 5.11: Reconstructed silhouette from an optimal circular array.

After 5.5 iterations, the resulting silhouette in Figure 5.11 is found. The circular array performed on par with the optimal string of pearls array in reproducing a perfect silhouette match. In addition, the circular array allows for multiple directions of shadow propagation, as opposed to a single direction for the string of pearls. The circular array's success may be a product of its increased measurements near the edges of the shadow. Recall that the Fresnel fluctuations are strongest near the edges and contain the most useful information there. Thus if a circular array is properly sized for asteroids of a given Fresnel number, the circular array will perform very well.

5.3.2 Non-Optimal Circular Configuration

The worst possible configuration of the circular array occurs when over half of the apertures become redundant, as shown in Figure 5.12. This happens when the shadow pattern moves across the array with an angle equal to integer values of the aperture separations.

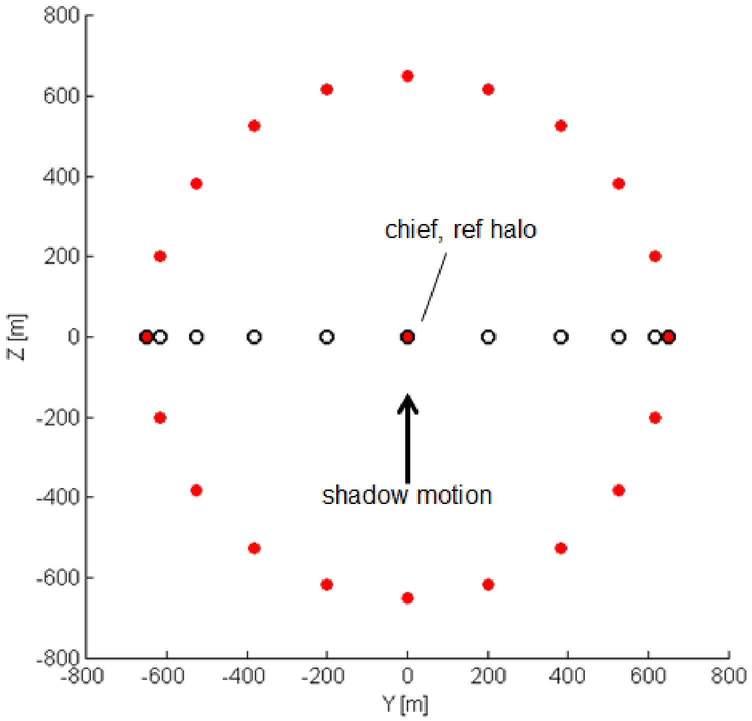

Figure 5.12: Non-optimal circular array with 21 evenly-spaced apertures.

As shown above, the number of useful apertures decreases from 21 down to 11. The pattern of data measured across the shadow pattern is shown in Figure 5.13. It is clearly evident that coverage of the observation plane has significantly decreased. Indeed, using this configuration there are not enough measurements taken across the shadow pattern to ensure process convergence within the allotted iterations. The resulting silhouette is shown in Figure 5.14 after 10 cycles.

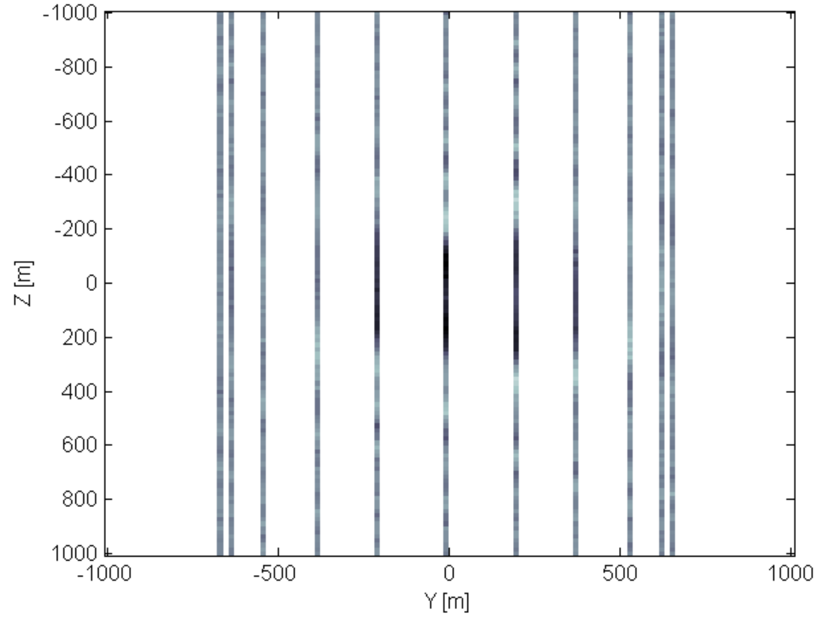

Figure 5.13: Sensor data swept out by non-optimal circular array.

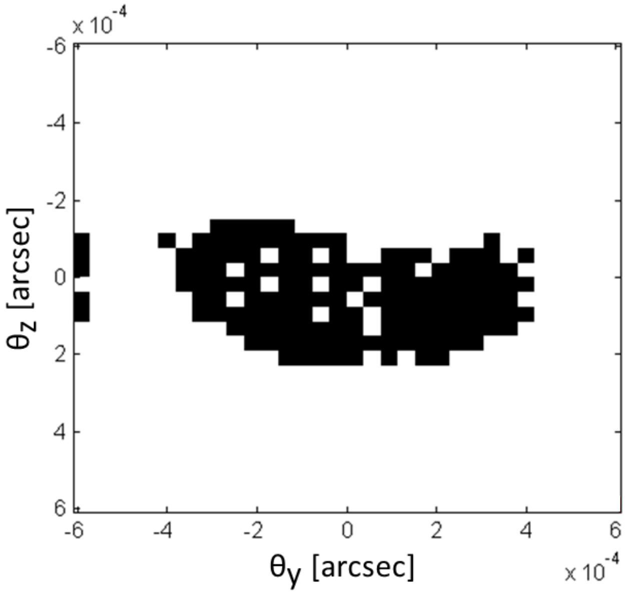

Figure 5.14: Reconstructed silhouette from a non-optimal circular array.

As expected, the resulting silhouette does not perfectly match the true pattern.

However, if it is assumed that the asteroid is solid, then the inside of the asteroid can be turned black and the extraneous pixels around the asteroid can be corrected so that the true silhouette is attained. The non-optimal circular array may not converge as quickly as the non-optimal string of pearls array, but it must be remembered that the actual worst case for the string of pearls provides no chance of silhouette reconstruction at all. Thus, this worst case circular array is still an effective option that is insensitive to shadow motion direction. In this respect, the circular array greatly outperforms the string of pearls.

In order for the worst case configuration to have the same data coverage as the optimal configuration, a total of 39 apertures would need to comprise the circular array. This was solved for using the following relation and a minimum of 20 apertures required in the worst case configuration.

$$N_{worst,circ} = \frac{N_{sat} - 1}{2} + 1 \tag{5.1}$$

where $N_{worst,circ}$ represents the number of usable apertures in the worst case configuration and N_{sat} represents the total number of apertures in the system.

5.4 Y-Shaped Array

The final array geometry simulated is the Y-shaped array. The 22 apertures are distributed equally along three arms with center at the reference halo orbit. Here 22 apertures are used instead of 21 to maintain the symmetry of this geometry. The chief aperture is placed on the reference halo center. The width of the array is measured from the tips of two arms. It was decided to use the shortest distance when meeting the array width requirement so that a minimum width in any direction was achieved. This makes the formation a bit more flexible with respect to the shadow size. The array lies in the yz-plane.

5.4.1 *Optimal Y-shape Configuration*

For the Y-shaped array, optimal performance makes use of all apertures in the formation. In order for this to occur, the shadow must move over the aperture with a small relative angle in the cross-track direction, such that no two sensors are redundant in measuring the light intensity. For a formation of 22 apertures, separated evenly along three arms, the formation geometry is shown in Figure 5.15.

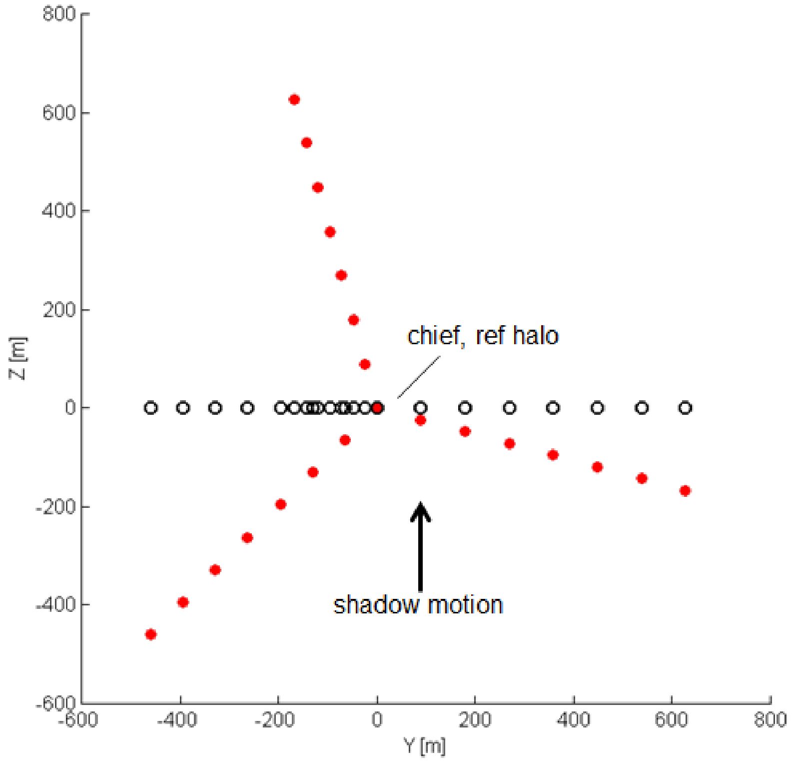

Figure 5.15: Optimal Y-shaped array with 22 evenly-spaced apertures.

The red points represent actual array positions, while the black circles show the projection of these positions onto the $\hat{y}$-axis perpendicular to shadow motion. The sensors sweep out data of intensity measurments as shown in Figure 5.16.

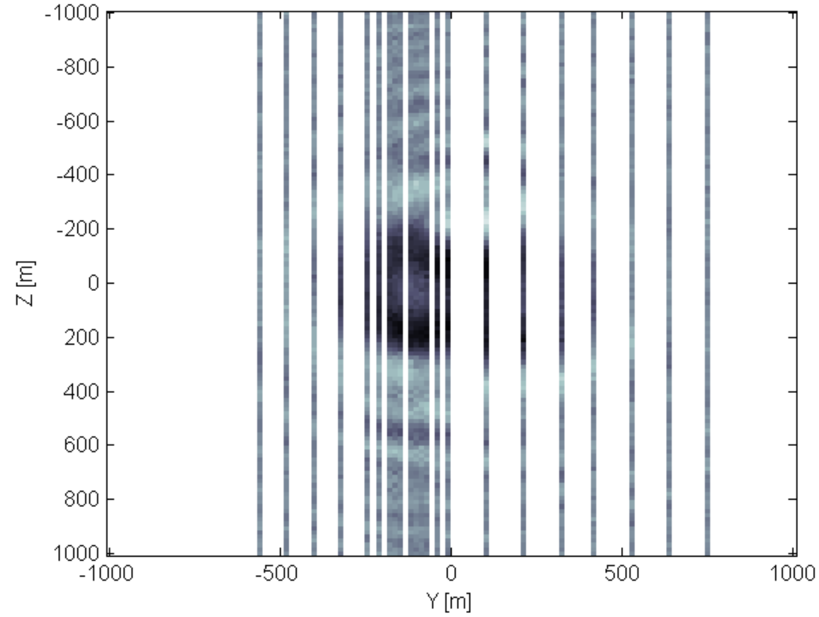

Figure 5.16: Sensor data swept out by optimal Y-shaped array.

As is the case for circular arrays, it should be noted that while all apertures appear to take non-redundant measurements of the shadow pattern, if the silhouette resolution is not fine enough, multiple aperture measurements contribute toward the same pixel estimations in the silhouette. The clustering of apertures at the neck of the Y (near the center of the shadow pattern) is a nominal consequence of the Y-shape geometry. Because of this clustering near the center, the additional apertures expected to improve convergence are not in fact as useful as those additional apertures in the circular array, which are more evenly distributed across the shadow pattern. In the circular array, the apertures have a greater chance of providing useful data for reconstruction, instead of overriding existing measurements with redundant ones. In addition, recall that Fresnel fluctuations are strongest near the shadow's edges. Because the clustering of sensors occurs in the neck region near the center of the shadow, these extra data points do not take advantage of the stronger data nearer edge.

After the maximum 10 iterations, the resulting silhouette in Figure 5.17 is found.

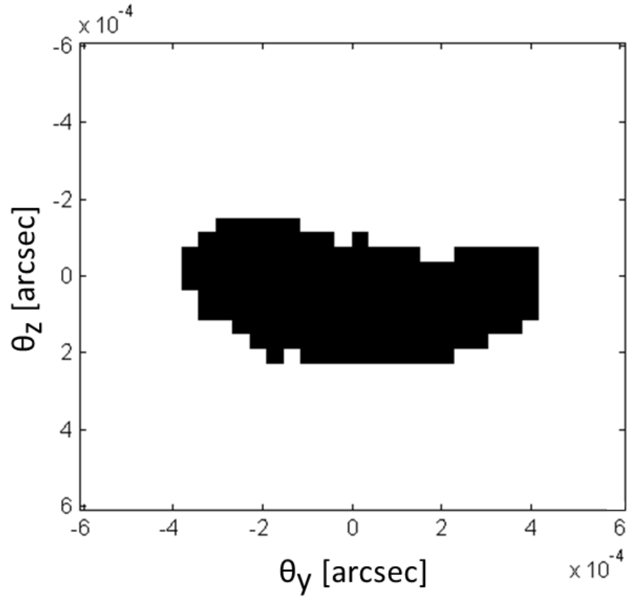

Figure 5.17: Reconstructed silhouette from an optimal Y-shaped array.

Despite a few extraneous pixels along the perimeter of the silhouette, the pattern matches closely with that of the true silhouette. This array geometry enables more shadow directions than the string of pearls, but appears to be less effective than the circular array. This is most likely due to its relative clustered distribution of apertures across the shadow pattern as opposed to the more evenly-spaced (edge-focused) distribution of the optimal circular configuration.

5.4.2 Non-Optimal Y-shape Configuration

The worst possible configuration of the Y-shaped array occurs when an entire arm of the array becomes redundant, as shown in Figure 5.18. This happens when the shadow pattern moves across the array with an angle equal to integer values of 30 degrees.

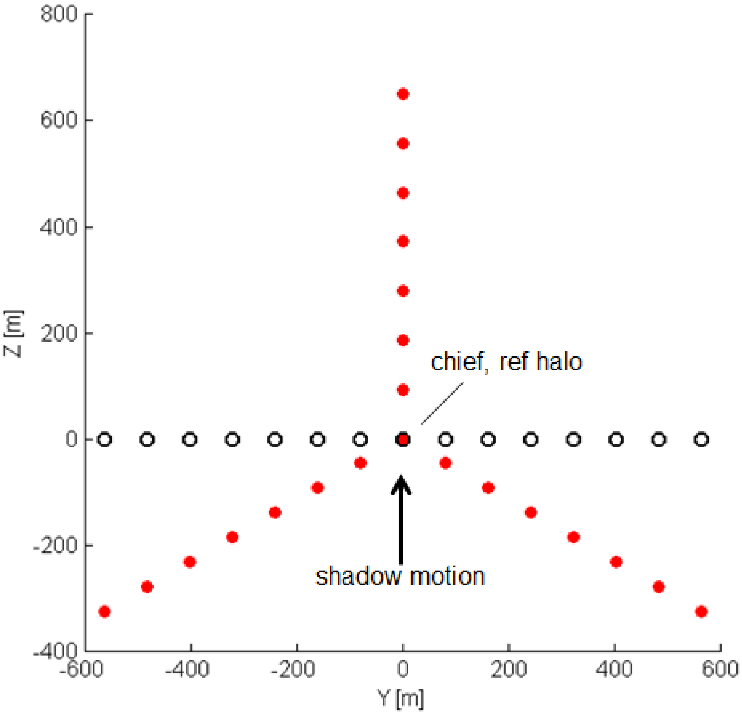

Figure 5.18: Non-optimal Y-shaped array with 22 evenly-spaced apertures.

As shown, the entire vertical arm becomes redundant, and the number of useful apertures decreases from 22 apertures down to 15 apertures. However, the distribution of points along the shadow pattern is more evenly-spaced than in the optimal configuration, where there is clustering around the neck of the Y. The pattern of data measured across the shadow pattern is shown in Figure 5.19.

The sensor pattern looks very similar to what would be expected from a string of pearls array with 15 evenly-spaced apertures. The resulting silhouette is shown in Figure 5.20, and resulted after the maximum 10 iterations.

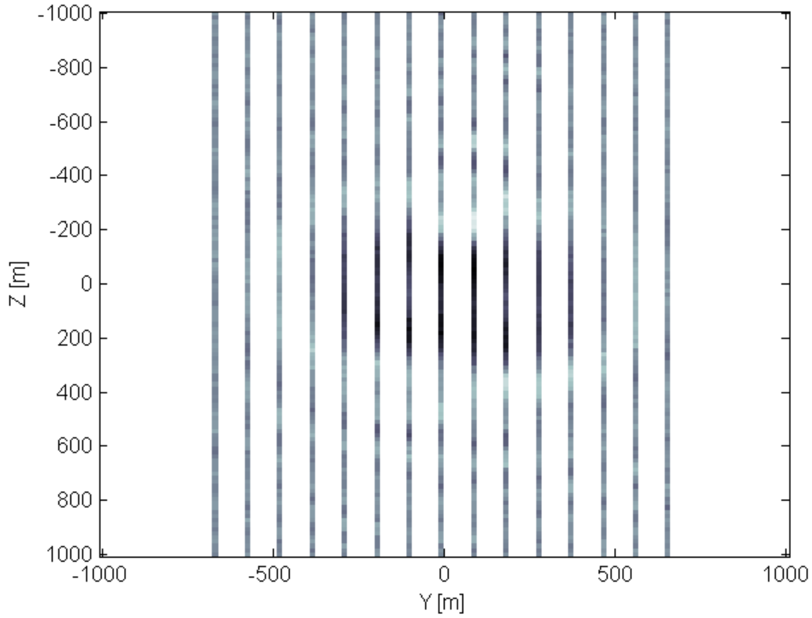

Figure 5.19: Sensor data swept out by non-optimal Y-shaped array.

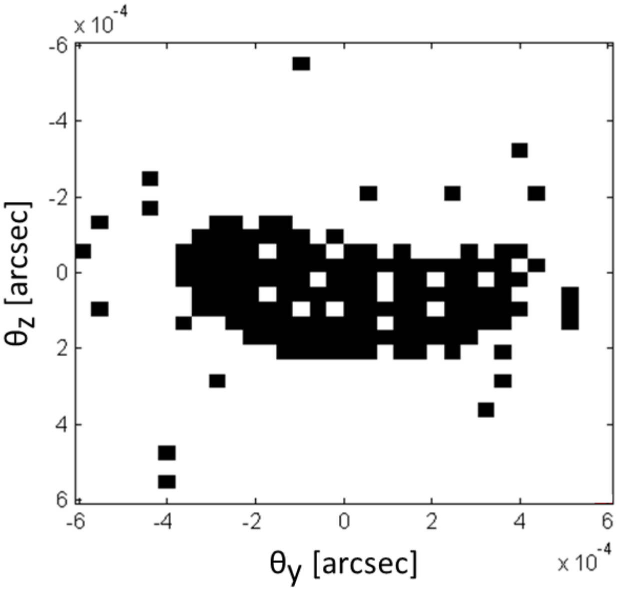

Figure 5.20: Reconstructed silhouette from a non-optimal Y-shaped array.

As expected, the worst configuration of the Y-shaped array did not produce a perfect silhouette pattern. However, the general shape of the asteroid is retained and could be used as an initial guess in future iterations.

If the Y-shaped array contains enough apertures in its worst configuration to have the required number of apertures across the shadow, the geometry is an effective system. A total of 30 apertures are required for the current example, given the following relation.

$$N_{worst,Y} = \frac{2(N_{sat} - 1)}{3} + 1 \tag{5.2}$$

where $N_{worst,Y}$ represents the number of useful apertures in the worst case configuration and N_{sat} represents the total number of apertures in the system.

While it appears that the Y-shaped array requires less apertures in this worse case configuration than that calculated for the circular array, it must be remembered that the optimal circular array out-performed the optimal Y-shaped array. However, constraints on implementing this occultation system in real life, such as limited budget and/or a maximum number of spacecraft available for manufacture, mean that the Y-shaped array could serve as a compromise between the string of pearls and circular array. Minimizing the number of required apertures while still enabling multiple directions of shadow motion, the Y-shaped array showcases the strengths of the other two geometries.

5.5 Imaging Simulation Conclusions

Several important results were discovered as a part of this system study. A string of pearls array provides excellent coverage of the shadow pattern in a single direction. The Y-shaped array provides for multiple directions of shadow motion; however, clustering of the satellites near the neck of the Y does not add useful measurements to the process. In addition, clustering coupled with relevant errors in aperture positions can complicate the process. A circular array provides the most versatile coverage of the shadow pattern due to its insensitivity to the shadow's velocity vector. Overall, evaluation of two new geometries (and extended analysis of another) have been added in support of advanced stellar occultation systems.

6. CONCLUDING REMARKS

Stellar occultation is widely used to characterize space-faring objects such as near Earth asteroids, moons and minor planets that pass in front of distant stars. However, the conventional method is limited in that it assumes the occulting object is large enough, or close enough, to cast a sharp shadow. For instance, smaller asteroids that are still large enough to cause severe damage to the Earth upon impact create shadow patterns that are heavily diffracted, making identification and characterization of them difficult. In this study, a novel space-based stellar occultation system is described which uses shadow diffraction principles to resolve silhouettes of these smaller asteroids. Past work has developed efficient algorithms which process the light intensity measurements of the shadow pattern, but aperture formation design has not been addressed until this thesis.

Libration point orbits are ideal locations for such imaging arrays, but require station keeping to maintain desired reference orbits. Thus, understanding control strategies for spacecraft in multi-body regimes is critical to the success of future space missions implementing imaging arrays at these locations. This study focused on spacecraft moving under the influence of multiple gravitational bodies, as modeled by the circular restricted three-body problem (CR3BP). First, the equations of motion for the CR3BP were developed and their unique properties explored. Five equilibrium solutions were found and named the libration points of the system. The problem was simplified by linearizing the equations of motion about the collinear libration points, and orbits unique to the libration points were examined, specifically periodic halo orbits. A differential corrections method was employed to solve for these periodic orbits, by varying the initial states such that the final targeted states were met.

Motion near the reference halo orbit is inherently unstable and requires station keeping algorithms to maintain the positions of apertures in the formation. A Proportional Derivative Controller, as well as a Linear Quadratic Regulator were derived and implemented for a formation of 21 apertures centered about the reference halo orbit. Three different array geometries were simulated–the string of pearls, circular, and Y-shaped arrays. Both the PD and LQR controllers were shown to maintain the desired formations with negligible errors and very low control effort–on the order of 10^{-11} N for a 100 kg spacecraft. Because station keeping errors were negligible with respect to the separation distances between apertures, analysis of silhouette reconstruction for various geometries could be carried out.

Previous work on the stellar occultation system has focused on silhouette reconstruction from knowledge of a shadow pattern of continuous data. In reality, the shadow pattern is only known at specified positions given by the aperture locations in the array at the time of occultation. This work furthered development of system requirements pertaining to data coverage and aperture positioning. Three array geometries were analyzed and compared for the novel occultation system described. A string of pearls was used as the base-line configuration, while the circular and Y-shaped arrays were used as alternative designs for comparison. For a given number of apertures, each array geometry was examined to find its best and worst configurations. Each configuration then underwent a simulation to reconstruct an asteroid silhouette given the light intensity measurements at each aperture.

The string of pearls array provides excellent coverage of the shadow pattern in a single direction. The circular array centered at the reference halo orbit was shown to have superior performance because of its insensitivity to the occulting shadow's velocity vector. Finally, the Y-shaped array was shown to be a viable compromise between the string of pearls and circular arrays by minimizing the number of apertures required but still enabling multiple directions of shadow motion. All of these examples presented in the current study further exhibit the requirement that for successful reconstruction of a silhouette, the number of apertures must be approximately equal to the number of pixels across the desired silhouette.

While this work furthered the capability and analysis of multi-aperture systems using stellar occultation, future work is needed to define more precise limits on the performance of each geometry. For instance, characterizing the maximum angle of shadow motion for effective silhouette reconstruction when using the string of pearls array. Future work should also involve investigations into using the natural dynamics associated with the reference halo orbit to further reduce the control costs of formation maintenance. It is believed that linearized dynamics associated with the halo orbit enable an array which rotates with the same orbital period as the halo orbit itself. Therefore, instead of holding the formation fixed with respect to the reference halo orbit, the formation would undergo a full rigid body rotation over the period of each orbit. In addition, requirements on fuel minimization and system lifetime studies should also be addressed.

REFERENCES

[1] L. Rayleigh, “XXXI. Investigations in optics, with special reference to the spectroscope,” *The London, Edinburgh, and Dublin Philosophical Magazine and Journal of Science*, vol. 8, no. 49, pp. 261–274, 1879.

[2] W. Traub, S. Shaklan, and P. Lawson, “Prospects for terrestrial planet finder (TPF-C, TPF-I, & TPF-O),” *Proceedings of the Conference In the Spirit of Bernard Lyot: The Direct Detection of Planets and Circumstellar Disks in the 21st Century*, June 2007. University of California, Berkeley, CA.

[3] S. Majewski, D. Law, A. Polak, and R. Patterson, “Measuring fundamental galactic parameters with stellar tidal streams and sim planetquest,” *The Astrophysical Journal*, vol. 637, no. 1, p. L25, 2006.

[4] P. Hariharan, *Basics of interferometry.* Academic Press, 2010.

[5] M. Born and E. Wolf, *Principles of optics: electromagnetic theory of propagation, interference and diffraction of light.* Cambridge University Press, 1999.

[6] R. Genet and B. Holenstein, “Alt-az light bucket astronomy,” *Lightweight alt-az telescope developments*, pp. 57–69, 2010. Santa Margarita.

[7] H. Brown and R. Twiss, “Interferometry of the intensity fluctuations in light,” *Proceedings of the Royal Society of London*, vol. 242, no. 1230, pp. 300–324, 1957.

[8] "Occultations." International Occultation Timing Association. Web. August 2014. <http://occultations.org/occultations/>.

[9] "Near Earth Asteroids." International Astronomical Union. Web. April 2013. <http://www.iau.org/public/nea/>.

[10] H. Altwaijry and D. Hyland, “Detection and characterization of near earth as-

teroids using stellar occultation," *AAS/AIAA Astrodynamics Specialist Conference*, August 11-15 2013. Hilton Head, South Carolina.

[11] R. Trahan and D. Hyland, "Phase retrieval applied to stellar occultation for asteroid silhouette characterization," *Applied Optics*, vol. 53, no. 16, pp. 3540–3547, 2014.

[12] W. Hartford, "Near earth asteroid detection system," *Foundary Team X Study, Jet Propulsion Laboratory*, May 9 2004. Pasadena, CA.

[13] J. Elliot, M. Person, C. Zuluaga, A. Bosh, E. Adams, and et al, "Size and albedo of kuiper belt object 55636 from a stellar occultation.," *Nature*, vol. 465, no. 7300, pp. 897–900, 2010.

[14] B. Sicardy, A. Bellucci, E. Gendron, F. Lacombe, S. Lacour, and et al, "Charon's size and an upper limit on its atmosphere from a stellar occultation.," *Nature*, vol. 439, no. 7072, pp. 52–54, 2006.

[15] B. Sicardy, A. Brahic, C. Ferrari, D. Gautiert, J. Lecacheux, and et al, "Probing titan's atmosphere by stellar occultation.," *Nature*, vol. 343, no. 6256, pp. 350–353, 1990.

[16] H. Schlichting, E. Ofek, M. Wenz, R. Sari, A. Gal-Yam, and et al, "A single sub-kilometre kuiper belt object from a stellar occultation in archival data.," *Nature*, vol. 462, no. 7275, pp. 895–897, 2009.

[17] F. Roques, A. Doressoundiram, V. Dhillon, T. Marsh, S. Bickerton, and et al, "Exploration of the kuiper belt by high-precision photometric stellar occultations: first results.," *Astronomical Journal*, vol. 132, no. 2, pp. 819–822, 2006.

[18] "Close-Up on the Asteroid Itokawa." Japanese Aerospace Exploration Agency. Web. August 2014. <http://global.jaxa.jp/article/special/hayabusa_sp3/index_e.html>.

[19] E. Young, "A fourier optics method for calculating stellar occultation light

curves by objects with thin atmospheres.," *Astronomical Journal*, vol. 144, no. 2, 2012.

[20] F. Roques, M. Moncuquet, and B. Sicardy, "A fourier optics method for calculating stellar occultation light curves by objects with thin atmospheres.," *Astronomical Journal*, vol. 93, pp. 1549–1558, 1987.

[21] D. Hyland and H. Altwaijry, "Asteroid characterization via stellar occultation: SNR calculation and observation opportunities," *AAS/AIAA Space Flight Mechanics Meeting*, January 26-30 2014. Santa Fe, New Mexico.

[22] R. Trahan and D. Hyland, "Mitigating the effect of noise in iterative projection phase retrieval," *Proceedings of the Imaging and Applied Optics: Optics and Photonics Congress*, July 2014. Seattle, WA.

[23] R. Trahan, "The phase retrieval problem and its applications in optics," December 2014. PhD dissertation. Texas A&M University, College Station, TX.

[24] R. Farquhar, "The control and use of libration point satellites," 1970.

[25] W. S. Koon, M. Lo, J. Marsden, and S. Ross, *Dynamical Systems, The Three-Body Problem, and Space Mission Design.* Marsden Books, 2006.

[26] V. Szebehely, *Theory of orbits: the restricted problem of three bodies.* Academic Press, 1967.

[27] B. Wie, *Space vehicle dynamics and control.* American Institute of Aeronautics and Astronautics, 2008.

[28] K. Howell, "Three-dimensional, periodic,'halo' orbits," *Celestial Mechanics*, vol. 32, no. 1, pp. 53–71, 1984.

[29] D. Richardson, "Analytic construction of periodic orbits about the collinear points," *Celestial Mechanics*, vol. 22, no. 3, pp. 241–253, 1980.

[30] S. Gordon, "Orbit determination error analysis and station-keeping for libration point trajectories," 1991. PhD dissertation. Purdue University, West Lafayette,

IN.

[31] L. D. Millard, "Control of satellite imaging arrays in multi-body regimes," 2008. PhD dissertation. Purdue University, West Lafayette, IN.

[32] S. Chakravorty, "Design and optimal control of multi-spacecraft interferometric imaging systems," 2004. PhD dissertation. University of Michigan, Ann Arbor, MI.

[33] I. Hussein and A. Bloch, "Dynamic coverage optimal control for interferometric imaging spacecraft formations," *43rd IEEE Conference on Decision and Control*, pp. 1812–1817, December 2004.

[34] G. Franklin, D. Powell, and A. Emami-Naeini, "Feedback control of dynamics systems," *Pretince Hall Inc*, 2006.

[35] F. Lewis and V. Syrmos, *Optimal control.* John Wiley & Sons, 1995.

[36] A. E. Bryson, *Applied optimal control: optimization, estimation and control.* CRC Press, 1975.